UNIVERSITY OF OKLAHOMA

GRADUATE COLLEGE

MODELING AND DESIGNING A VERTICAL ISOLATION SYSTEM USING A LATERALLY LOADED ARCH AS A NEGATIVE STIFFNESS ELEMENT

A THESIS

SUBMITTED TO THE GRADUATE FACULTY

in partial fulfillment of the requirements for the

Degree of

MASTER OF SCIENCE

By

STONE L. BRACKETT
Norman, Oklahoma
2022

MODELING AND DESIGNING A VERTICAL ISOLATION SYSTEM
USING A LATERALLY LOADED ARCH
AS A NEGATIVE STIFFNESS ELEMENT

A THESIS APPROVED FOR THE
SCHOOL OF CIVIL ENGINEERING AND ENVIRONMENTAL SCIENCE

BY THE COMMITTEE CONSISTING OF

Dr. Philip Scott Harvey Jr., Chair

Dr. Royce W. Floyd

Dr. Shreya Vemuganti

This thesis is dedicated to my brother, Smoky Brackett, who passed away in December 2019. Thank you for always driving me into being the best me through our competitive natures.

Acknowledgements

I would like to acknowledge several people and entities for their support of my work, both on this research and throughout my time at OU.

This material is based upon work supported by the National Science Foundation under Grant No. CMMI-1943917. Thank you to the National Science Foundation for helping to fund this opportunity for me to learn through experimentation. The opinions expressed in this thesis are those of the author and do not necessarily reflect the views of the sponsor.

Thank you to Dr. Scott Harvey for being a fantastic professor and advisor who has helped me grow into the engineer that I am today. His work, both as a professor and a mentor, allowed me to effectively understand the important concepts that structural dynamics and isolation are based on.

Thank you to Dr. Royce Floyd and Dr. Shreya Vemuganti for serving on my committee and taking the time out of their schedules to carefully review my work and give me important feedback, helping me to improve as a writer and a thinker.

Thank you to Thomas Cain and Esteban Villalobos Vega for assisting me with my research and for helping to teach me about the inner-workings of isolation systems.

Thank you to my professors and TAs throughout OU who have taught me not only the important engineering material, but how to learn and ask questions. I would especially like to thank Dr. John Albert, Dr. Samuel Duwe, Dr. Floyd, Dr. Harvey, Dr. Robert Lifset, Dr. Bruce Mason, Dr. Jinsong Pei, Dean Gary Raskob, Mr. Steve Roswurm, and Dr. Keith Strevett for going above and beyond as teachers to motivate me to not only

learn the content in their courses, but to thoroughly enjoy the course and connect with the material.

Thank you to my friends who I made freshman year who have been with me throughout college, Ethan Brody, Brett Francis, Tim Gehrsitz, Ben Gochanour, Paxton Leaf, Jacob Luft, James Martindale, Alex Parsells, Perry Powell, Bryce Rombach, Nathan Woo, and Jordan Zimmerman. I'd also like to thank my freshman year RA, Erik Fretland, for not only being a fantastic friend but also a great role model for me over the course of the last few years. I'm super thankful for all of the memories I've been able to form with these guys over the course of the last few years. They have been a constant source of knowledge, advice, and of course entertainment for me throughout college.

Thank you to Taylor Swift for providing me thousands of hours of entertainment throughout school through her music. She helped me get through some of the more boring times of life, including COVID in 2020 through 2021 when I tended to be more reclusive.

Lastly, thank you to my family for supporting me throughout school. I am especially thankful to my mom, Maureen Brackett, who puts up with me being gone for several months at a time and not always doing the best job at keeping in touch. Thank you for everything you've done for raising me into the man I've become today, educationally and morally.

Table of Contents

List of Figures

List of Tables

Abstract

Structures, artwork, and expensive equipment are often susceptible to significant damage from vertical dynamic motion such as that generated by earthquakes. Several systems exist which seek to mitigate damage caused from motion, but the study of vertical dynamic motion isolators lags behind that of horizontal motion isolators. This thesis explores the design of a vertical isolation system utilizing two laterally loaded arches, acting as beams, to generate negative stiffness. This negative stiffness is counteracted by a positive, linear stiffness from a parallel spring to create a quasi-zero stiffness. The quasi-zero stiffness shifts the natural frequency of the system to almost zero, causing frequency ratios experienced by the system to approach infinity. As a result, the system experiences low transmissibility from the base of the system to the point of interest, which in the case of this research is at the connection joining the beams to which the isolated mass is attached. Essentially, it allows for this connection to be effectively isolated from the effects of vertical accelerations at the base of the system.

Both an experimental prototype and two different theoretical models are examined in this thesis, which allows for a physical system to be compared to theories in order to determine the efficacy of the system and to help validate the theories. The experimental prototype is produced with a focus on using lightweight materials and allowing for a low profile. In order to achieve this goal, 3D printed parts are used. This allows for high levels of control when designing for different system variables such as the length of the beams, the stiffness of the beams, and the initial rise of the beams. Static testing is performed on the prototype to characterize properties of the beam and spring and

to optimize the system. This is done simultaneously alongside the development of the two theoretical models, which aimed to aid in and simplify the design process, as beam properties could be roughly determined before being 3D printed. MATLAB is used in combination with OpenSees in order to test the different theoretical models before they are fabricated on the 3D printer. As static testing is performed, changes to the system are made in order to both improve system performance and calibrate it for future dynamic testing. Following the completion of the static testing and the implementation of small modifications into the system, dynamic testing is performed using a vertical shake table to evaluate the isolation performance of the system. The motions the system is subjected to are a variety of harmonic excitations at different frequencies and amplitudes and white noise. The accelerations of the isolated mass are measured. This then allows for the isolation performance of the system to be determined by comparing the accelerations experienced by the mass to the accelerations at the base of the system. A comparison of the experimentally determined results and the theorized results is performed and will be used for the development of future research, including the development of systems similar to the one discussed in this research.

Chapter 1
Introduction

1.1 Project Information

1.1.1 Background

This project is a continuation of the research performed by Thomas Cain for his master's thesis (Cain, 2020) under Dr. Harvey. That research focused on designing a vertical isolation system using 3D printed materials. It aimed to create a system that was small and had a low profile, in the idea that it could be scaled up at a later time. The vertical isolation system designed in that research had several flaws related to the stability of the system, for example the beam had sudden snap-through as loading progressed, resulting in high accelerations. Also, the pinned boundary conditions were difficult to achieve, and creep was observed in the buckled beam. In this thesis, information learned from Mr. Cain's thesis is utilized to design a better system that fixes some of the flaws noticed in that system. Information pertaining to Mr. Cain's thesis is found in Appendix A.

1.1.2 Motivation

There are several types of isolation systems, including horizontal isolation systems which resist horizontal motion and vertical isolation systems which resist vertical motion. The system considered in this research is a vertical isolation system. For reference, the system discussed in this research can be seen in Figure 1.1.

Understanding the workings of vertical isolation systems has several practical ap-

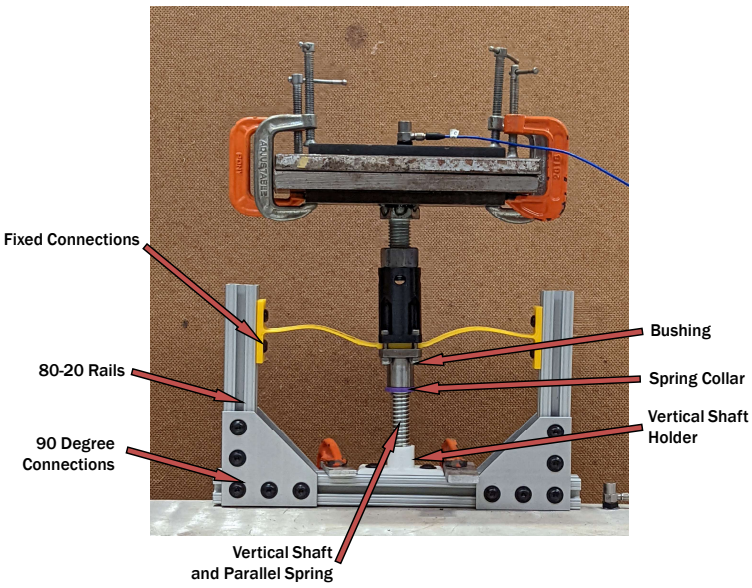

Figure 1.1: Test system discussed in this research.

plications. One of the primary situations where vertical isolation systems are useful is in earthquake mitigation. Systems are used in practice in high seismic zones in order to reduce destruction caused by earthquakes. Smaller scale systems can be used to protect objects from a variety of different dynamic motions, including earthquakes, transportation-related accelerations, and movement of heavy machinery and heavy transportation such as trains. Examples of objects that could be protected with a system such as the proposed one include artwork, biomedical equipment, telecommunications equipment, silicon manufacturing equipment, and other valuables (Tehrani and Harvey, 2019).

1.1.3 Basic Theory

One of the important variables this research examines and utilizes is stiffness. In this research's isolation system, stiffness is a function of several different components, including beam thickness, beam length, beam camber (rise), and the current load on the beam. In this research, the terms "beam" and "arch" are used interchangeably. An arch

refers to a beam with an initial curvature while still being stress-free. Stiffness has a direct impact on the dynamic motion of the system. This is due to the stiffness affecting the way the structure reacts to different accelerations, and consequently different forces. A quasi-zero stiffness, or a stiffness that is approaching zero, is used in this research in order to achieve isolation (Lan et al., 2014; Zhou et al., 2019). This quasi-zero stiffness is attained from the usage of two laterally loaded arches, which provides negative stiffness, and a parallel spring, which provides positive stiffness.

For the dynamic testing portion of the experiment (Chapter 4), acceleration is the primary dependent variable measured. In order to attain isolation and prove the theory, the system needs to experience significantly reduced acceleration at the top, where the payload is located, despite there being an acceleration applied at the bottom.

1.1.4 Scope

The system this thesis discusses is intended to protect smaller objects, not necessarily structures. However, a comparison of the proposed system to those in use for structures would show similar concepts in design. Future iterations of the design will need to be slimmed down further in order to fit this purpose better.

1.2 Literature Review

1.2.1 Stiffness

Stiffness is the primary mechanism through which the vertical isolation system designed in this experiment functions. It explains and predicts how a material will deform under a load. Deformation can be a critical component of evaluating a structure's performance because many materials have deformation limits. For example, concrete has a maximum allowable deflection according to the American Concrete Institute code. Stiffer materials are better able to resist deflections, meaning that they move less. Essentially, stiffness is the slope of the load-deflection curve (Baumgart, 2000).

Stiffness is a property that can be adjusted based on many different factors, including but not limited to shape, end condition, and the type of material. Numerous studies have been performed on all of these different properties in order to understand the effect of these on stiffness (Klasson et al., 2016; Leavitt et al., 2007; Baumgart, 2000; Yan et al., 2018). For example, Porter et al. (2019) performed a three-point bending test on 3D printed beams in order to determine the effect of infill on stiffness. 3D printed beams similar to those tested in Porter et al. (2019) are used in the research discussed in this thesis.

Another important consideration regarding stiffness is its effects on dynamic motion of structures. Some important natural phenomena that often result in large amounts of destruction are earthquakes. The study of isolation systems and their effects on reducing the damage incurred by earthquakes dates back over 100 years (Schaer, 1909; Harvey and Kelly, 2016). Only recently, however, have isolation systems begun to be used to counteract the forces and accelerations created by earthquakes in tall buildings (Buckle and Mayes, 1990). Earthquakes generate rapid forceful motion, often shifting direction quickly. One contributing factor to an earthquake's destruction is its frequency, and more importantly its comparison to nearby buildings' natural frequencies. Natural frequencies are an important factor regarding dynamic motion as they can affect the amplitude, or the amount of acceleration (and thus force), transmitted to the building. The ratio of how much acceleration is transmitted to the structure is also known as the transmissibility of a structure. Natural frequencies can be calculated using a building's mass and stiffness properties. If the frequency of seismic activity (or any dynamic loading) is close to that of the natural frequency, then the acceleration of the building will increase, oftentimes resulting in increased damage (Szolomicki and Golasz-Szolomicka, 2019). The ratio between a structure's forcing frequency and natural frequency is its frequency ratio, β. As β approaches infinity, the structure's transmissibility approaches zero, as

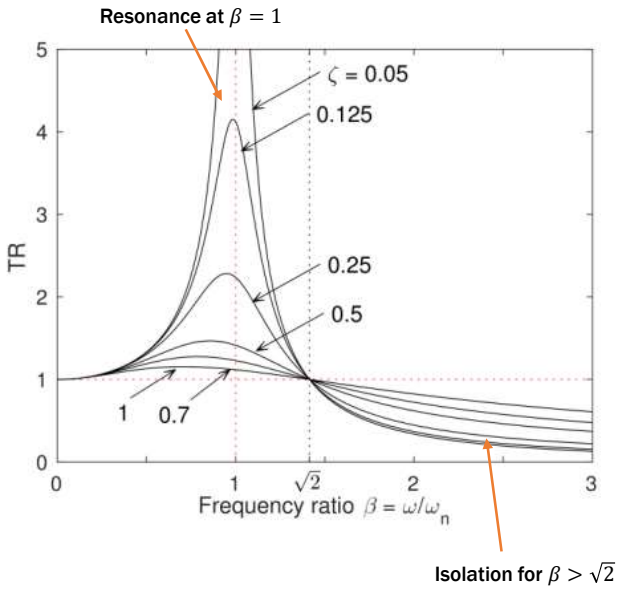

Figure 1.2: Transmissibility (TR) versus frequency ratio β for different damping ratios ζ.

can be seen in Figure 1.2. This is the basis of how stiffness affects the accelerations an object sustains.

As was noted above, one important component in calculating natural frequencies is stiffness. Natural frequencies are a function of stiffnesses ($\omega_n = \sqrt{k/m}$), meaning that as a stiffness approaches zero, the corresponding natural frequency will approach zero. Having a very low stiffness will result in structures having an incredibly low amplification, and thus minimally experiencing the high accelerations due to an earthquake. One such way to obtain this low stiffness is through having stiffnesses that cancel out, such as by using a spring and an arch or buckled beam. A buckled beam exhibits a negative stiffness, whereas a spring exhibits a positive, linear stiffness. When these two stiffnesses are added together, this generates the property of quasi-zero stiffness (Wang et al., 2020).

1.2.2 Stiffness with Regards to Laterally Loaded Arches

One way to analyze a structure's stiffness is through a force-displacement curve. This will give important information about the stiffness of a structure, as stiffness can be defined as the derivative of the force-displacement curve with respect to displacement. This stiffness can then be used to determine different properties about the material; for example springs have a linear stiffness (Zhou et al., 2019). This can be seen in a force-displacement curve for a spring as a straight line with positive slope. Force-displacement curves for more complicated structures, such as transversely loaded buckled beams or arches, can have more variance.

One structural element that has been studied for a long time is the usage of a laterally loaded arch to provide stiffness, as the force-displacement curves of arches have multiple equilibrium configurations. Laterally loaded arches have been studied for several decades, with tests on their usage as a structural component and their stiffness dating back to the 1970s (Pi et al., 2007; Harrison, 1978; Iwan, 1978). Laterally loaded arches have a force-displacement curve that increases, then has a downwards slope as it snaps-through to a different equilibrium point, and then continues to increase again (Figure 1.3). As the arch snaps through it exhibits negative stiffness. The properties of the laterally loaded arch are not constant among all cases, however. The deflected shape of a laterally loaded arch varies based on several conditions including end shortening, which affects the amount of rise in the arch and thus the stiffness, and end conditions, which affect the way the arch buckles as well as how much of a harmonic is represented in the arch (Harvey and Virgin, 2015; Harvey et al., 2020). System properties such as the operating load and the magnitude of the negative stiffness are affected by the aforementioned properties of the laterally loaded arch as well as other properties of the arch resulting from the material and the shape of the arch.

Another important component of the laterally loaded arch in the context of isolation

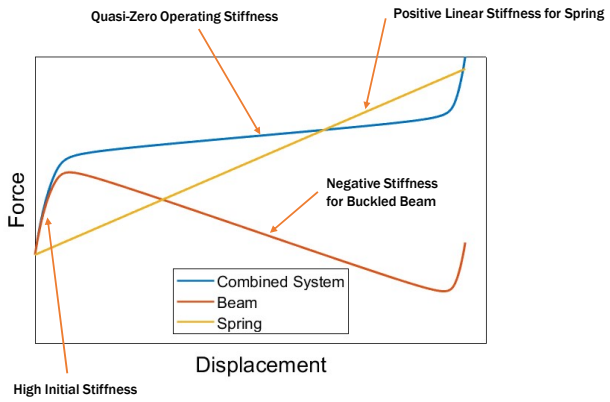

Figure 1.3: Force-displacement curve for a generic laterally loaded arch exhibiting snap through and negative stiffness. Additionally contains stiffness for a spring and for the combined system, composed of two beams and a spring.

systems is the high initial stiffness exhibited by the arch. This can be seen in Figure 1.3 as the high initial slope as displacement is initially increasing. This high initial stiffness allows for more desirable (i.e., lower) static load deflections in many cases when compared to other systems with low stiffness, such as in the case of a soft spring. This is because the initial loading that is applied has less settlement than if the entire range of the system exhibits quasi-zero stiffness. While this does complicate the design of the vertical isolation systems, it improves the characteristics and footprint of the isolation systems. More specific details about how the shape of the arch (in terms of buckled mode) affects the stiffness of the arch can be found in Chapter 2.

1.2.3 Isolation Systems

The negative stiffness of the laterally loaded arch is important when combined with other elements in an isolation system, such as a spring. The stiffnesses from the different structural components of the system can be added together to generate a combined force-displacement curve, and with it a combined stiffness. This combined stiffness is then responsible for affecting the structure's dynamic responses, which can result in reduced accelerations and transmissibility from potentially harmful dynamic motions,

such as earthquakes. This setup of the laterally loaded arch in combination with a spring, which seeks to create quasi-zero stiffnesses in order to mitigate the effects of earthquakes, is a form of isolation system.

Isolation systems themselves are not a new topic of study. Seismic mitigation techniques have been employed since the 1960s for tall buildings such as the World Trade Center which used a passive damping system in order to reduce its transmissibility and thus its dynamic motion (Lago et al., 2018). Since then, more complicated isolation systems have been built. One company, Minus K, creates an isolation system that protects against several different types of motion, including vertical motion, horizontal motion, and vibrations. This system, however, is very large and complicated. A small-scale system designed for vertical isolation is still not on the market. Vertical isolation systems compose an emerging field of study which has begun to have more research performed on it in recent years. Research on vertical motions in structures has begun to be seen as increasingly important when evaluating the dynamic performance of a structure. For example, Cui et al. (2012) recommended an increase in the amount of research allocated to the vertical motions of structures after analyzing the performance of a building using a structural fuse system.

Most vertical isolation systems seek to use quasi-zero stiffness in order to mitigate the effects of vertical forces, which is important as earthquakes generate forces in both planes of movement. There are several different examples of systems that exhibit properties similar to those of vertical isolation systems. One specific example, which can be found as part of the natural world, is chicken necks (Deng et al., 2020). Additionally, springs in cars can exhibit similar negative stiffness properties (Lee et al., 2007). However, despite different systems involving negative stiffness existing, few have been developed into a working small-scale vertical isolation system. Several different vertical isolation systems have been explored. Different studies use a variety of different

designs, including varying methods, end-conditions, and layouts. Many systems consist of springs working in combination with a buckled beam in order to simulate a quasi-zero stiffness, such as those researched in Lee et al. (2007), Liu et al. (2013), and Fulcher et al. (2014a). Significant numerical analysis has been performed on quasi-zero stiffness systems and their performance has been determined to be helpful for isolating buildings from seismic excitations (Zhou et al., 2019).

Research into isolation systems similar to the one discussed in this research has been performed by others. For example, Zhou et al. (2019) created an isolation system using two disc springs as negative stiffness elements. This system differed from the one discussed in this research in that the negative stiffness elements have different properties and the conditions used in that study are pinned conditions, adjusting the characteristics of the system. Fulcher et al. (2014b) explored a system that used a buckled beam with fixed end conditions and a linear spring in parallel. However, this study examines a beam that is stressed as it is buckled into its first mode deflected shape rather than a laterally loaded arch, resulting in different behavior than that examined in this research.

A simple spring with a low stiffness could be considered to cause isolation as well, as the low stiffness created by the spring allows for large displacements without transmitting large amounts of force. However, the issue with using low stiffness springs lies in large static displacement due to dead (gravity) loads from the isolated mass. The high initial stiffness of the laterally loaded arch in parallel with a spring allows for load to be applied before reaching the quasi-zero stiffness range of the force-displacement curve. This causes a lower static deflection in systems using the laterally loaded arch.

1.2.4 Seismic Mitigation

Vertical isolation devices could have significant implications in reducing the damages caused by seismic motion. Vertical components of seismic waves are still being studied in order to better understand them. Vertical accelerations can have large variances

when compared to horizontal accelerations at the surface of an earthquake. Oftentimes the effects of vertical acceleration is underestimated in engineering applications (Yang et al., 2002). As vertical acceleration is a key component of vertical isolation systems, the research of vertical accelerations induced by seismic waves and vertical isolation systems are closely related.

Seismic motion can have drastic effects on different structures. One example is the effect on bridges. Bridges can be damaged beyond repair in the event of large earthquakes. The effects of vertical motion from earthquakes are often not considered in the design of bridges. The vertical motion from earthquakes can increase the shear force generated from the earthquake by as much as 50%. The vertical shear force generated by earthquakes is often unaccounted for in the design of bridges. This failure to account for the design of vertical motion could result in increased damage (Kalantari and Moayyedi, 2018). Accounting for this vertical motion has only recently made its way into codes, with it first appearing in loading considerations in ASCE 7-16 (ASCE, 2017). The consideration of vertical motion in design will help to improve infrastructure going forward as further understanding of the mitigation strategies are developed.

Vertical isolation systems have been found to be helpful in mitigating the effects of seismic motion. Following the events of Fukushima in 2011, research was performed in an attempt to help prevent a disaster of that magnitude. Several vertical isolation systems were tested in order to evaluate their performance. It was concluded from the research that the usage of vertical isolation systems in a nuclear power plant would be helpful in preventing future disasters (Najafijozani et al., 2020).

1.3 Summary

In summary, this research evaluates how well a small-scale vertical isolation system with a pair of laterally loaded arches and springs achieves quasi-zero stiffness and, ultimately, isolation. Additionally, this research attempts to form a basis and working

model for future tests involving vertical isolation. Several distinct steps will be performed in order to complete this research, both in design and testing, which are outlined in this thesis. In Chapter 2, a mathematical energy minimization approach and OpenSees model are used to predict the behavior of the test setup. Then, in Chapter 3, a physical prototype is created and the results from Chapter 2 are verified experimentally using this prototype. Then, in Chapter 4, this physical prototype is subjected to dynamic motion in order to determine the isolation performance of the test setup. Finally, in Chapter 5, conclusions about the test setup are made and future tests and work are proposed.

Chapter 2
Theoretical Models

2.1 Overview

In order to evaluate the vertical isolation system examined in this research two different theoretical models are used. The first model involves using energy minimization in order to find stable beam shapes for different displacements. This is then used to calculate the displacement at different shapes, as well as the load required to achieve the target displacement. The second model involves using OpenSees (McKenna and Feneves, 2000), an earthquake simulation software created by researchers at the University of California, Berkeley, in order to impose displacements on a structure and calculate the corresponding loads/reactions. These models' results will then be compared to one-another in order to determine whether there is consistency between the models.

2.2 Energy Minimization Approach

The first method that is used for modeling the behavior of the beam is an energy minimization approach. This method uses the strain energy stored in the beam by looking at the buckled shape of the beam as increasing displacement is imposed. From there, the beam takes the shape with the lowest strain energy as that is the most stable. Using constraints from the end conditions, one can solve for the minimum energy state of the beam for given displacements. From this, the shape of the beam can be determined and thus the loading required to achieve a given displacement and a force-displacement

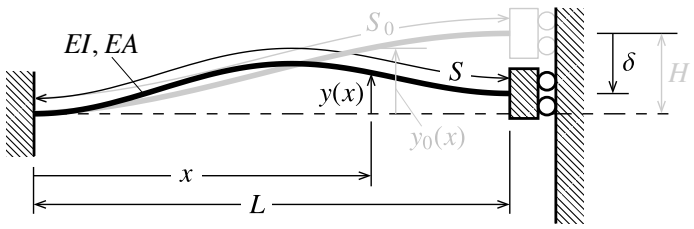

Figure 2.1: Geometry and description of an arch: The undeformed beam (gray) of span L, arc length S_0, rise H, flexural rigidity EI, and axial rigidity EA takes the initial shape $y_0(x)$. After imposing an end displacement δ, the beam takes the shape $y(x)$ (black) of arc length S.

curve.

2.2.1 Energy Minimization Framework

Consider the beam of span L, shown in Figure 2.1. The initial lateral, stress-free shape $y_0(x)$ is assumed shallow, and the beam is assumed homogeneous and uniform with flexural rigidity EI and axial rigidity EA. The initial "rise" at the right-hand end is $y_0(L) = H$. Now a lateral constraint is imposed at the right-hand end ($x = L$) such that the lateral deflection $y(L) = H - \delta$ (Figure 2.1), where $y(x)$ is the general deflected shape and δ ($\downarrow_+$) is the deflection at $x = L$. This constraint is taken here to be fixed, where neither rotation nor horizontal translation at L are not allowed; however, vertical translation is allowed. For $x = 0$, the constraint is taken to be entirely fixed, where no rotation or translation in any direction is allowed. The shape of the beam is highly influenced by the end conditions imposed on the beam. The beam considered in this research's experimental tests (Chapters 3 and 4) to provide negative stiffness is similar to that described in Figure 2.1.

For a general deflected shape $y(x)$, the arc length S of the beam midline is given by

$$S[y(x)] = \int_0^L \sqrt{1 + [y'(x)]^2}\, dx \approx \int_0^L \left\{1 + \frac{1}{2}[y'(x)]^2\right\} dx = L + \frac{1}{2}\int_0^L [y'(x)]^2\, dx. \quad (2.1)$$

The midline axial deformation Δ of the beam is given by

$$\Delta[y(x)] = S_0 - S[y(x)] \quad \text{(shortening positive)} \quad (2.2)$$

where $S_0 = S[y_0(x)]$ is the arc length of the initial, unstressed deflected shape. The curvature χ of the beam is given by

$$\chi[y(x)] = \frac{y''(x)}{\{1 - [y'(x)]^2\}^{1/2}} \approx y''(x) \tag{2.3}$$

The total elastic strain energy U in the beam for the deflected shape $y(x)$ can be expressed as (Thompson and Hunt, 1983)

$$U[y(x)] = \frac{1}{2}EI \int_0^L \{\chi[y(x)] - \chi[y_0(x)]\}^2 \, dx + \frac{1}{2}\frac{EA}{S_0}\{\Delta[y(x)]\}^2 \tag{2.4a}$$

$$\approx \frac{1}{2}EI \int_0^L [y''(x) - y_0''(x)]^2 \, dx + \frac{1}{2}\frac{EA}{S_0}\Big\{S_0 - L - \frac{1}{2}\int_0^L [y'(x)]^2 \, dx\Big\}^2 \tag{2.4b}$$

Stable equilibria exist when the minima of the strain energy occur, and this minimization is subject to the lateral constraint, which can be expressed as follows:

$$\begin{cases} \min\limits_{y(x)} & U[y(x)] = \dfrac{1}{2}EI \displaystyle\int_0^L [y''(x) - y_0''(x)]^2 \, dx + \dfrac{1}{2}\dfrac{EA}{S_0}\Big\{S_0 - L - \dfrac{1}{2}\displaystyle\int_0^L [y'(x)]^2 \, dx\Big\}^2 \\ \text{s.t.} & y(L) = H - \delta \end{cases} \tag{2.5}$$

The constraint equation (i.e., $y(L) = H - \delta$) is for the fixed lateral constraint assumed in this study, but other constraint conditions could alternatively be considered by modifying this constraint equation, e.g., $y(L) \leqslant H - \delta$ for unilateral constraint (Plaut, 2015; Harvey and Virgin, 2015).

A solution to the minimization problem (Equation (2.5)) is sought using a multiplier method, wherein multiplier λ is used to enforce the lateral-constraint equation. The lateral-constraint equation is multiplied by λ, which is then added to the strain energy equation to provide an augmented strain energy function, $U_a \equiv U_a[y(x), \lambda]$, which will be maximized over the multipliers and minimized over the shape, as described by

$$\min_{y(x)} \max_{\lambda} U_a[y(x), \lambda] = \frac{1}{2} EI \int_0^L [y''(x) - y_0''(x)]^2 \, dx + \frac{1}{2} \frac{EA}{S_0} \left\{ S_0 - L - \frac{1}{2} \int_0^L [y'(x)]^2 \, dx \right\}^2 + \lambda \left[y(L) - (H - \delta) \right] \quad (2.6)$$

The physical interpretation of multiplier λ is the lateral force required to be applied at $x = L$ that strictly enforces the constraint.

The general expression for the deflection curve can be expressed by the series

$$y(x) = \sum_{n=1}^{\infty} Q_n \psi_n(x) \quad (2.7)$$

where $\psi_n(x)$ = a shape function consistent with the boundary conditions, and Q_n = the associated coefficient. The initial shape can be expanded using the same basis functions:

$$y_0(x) = \sum_{n=1}^{\infty} Q_{n,0} \psi_n(x) \quad (2.8)$$

where $Q_{n,0}$ are the associated (known) coefficients. Substituting these forms of $y(x)$ and $y_0(x)$ into Equation (2.5), the minimization problem is in terms of the unknown coefficients Q_n, as discussed in the following section.

2.2.2 Fixed-End Beam Expansion

For the case of a fixed-end beam, first the axial deformation in the beam needs to be determined. To do this, the arc length is determined by using a truncated Fourier series with only three retained terms to determine the shape of the beam, $y(x)$, in terms of coefficients Q_1, Q_2, and Q_3 in combination with harmonic terms representing mode shapes. As the beam has fixed-end conditions, constraints are imposed on the shape function such that there are no rotations at either end of the beam, no horizontal deformations at either end of the beam, and no vertical deformations at the outside end of the beam

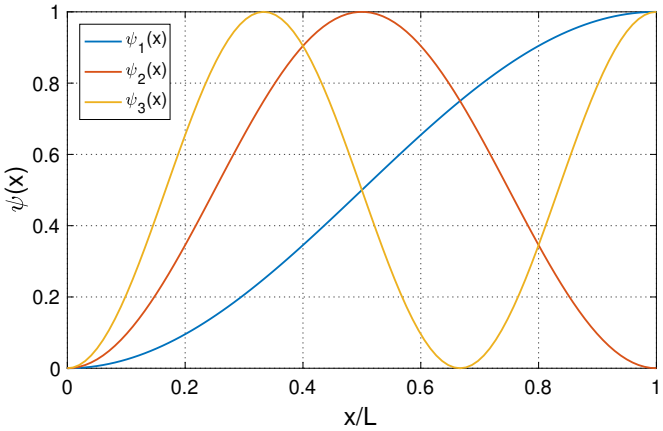

Figure 2.2: Shape functions $\psi_n(x)$ used in the fixed-end beam expansion of $y(x)$.

($x = 0$). This results in the following mode shapes:

$$\psi_1(x) = \frac{1}{2}[1 - \cos(\pi x/L)] \tag{2.9a}$$

$$\psi_2(x) = \frac{1}{2}[1 - \cos(2\pi x/L)] \tag{2.9b}$$

$$\psi_3(x) = \frac{1}{2}[1 - \cos(3\pi x/L)] \tag{2.9c}$$

which are depicted in Figure 2.2. The arc length can then be determined by using Equations (2.1), (2.7), and (2.8) to be

$$S = L + \frac{\pi^2({Q_1}^2 + {Q_2}^2 + {Q_3}^2)}{16L} \tag{2.10}$$

and

$$S_0 = L + \frac{\pi^2({Q_{1,0}}^2 + {Q_{2,0}}^2 + {Q_{3,0}}^2)}{16L} \tag{2.11}$$

where $Q_{1,0}$, $Q_{2,0}$, and $Q_{3,0}$ are the shape function coefficients associated with the initial beam shape ($Q_{n,0}$).

After determining the arc length, S, for both the initial condition and the deformed condition, the two arc lengths can be subtracted from one another in order to determine the axial deformation using Equation (2.2). For the case of the fixed-fixed beam, axial

deformation is given by

$$\Delta = \frac{\pi^2}{16L}[{Q_1}^2 - {Q_{1,0}}^2 + 4{Q_2}^2 - 4{Q_{2,0}}^2 + 9{Q_3}^2 - 9{Q_{3,0}}^2] \tag{2.12}$$

where $Q_{n,0}$ represents Fourier coefficient of the initial shape of the beam.

After determining the axial deformation of the beam, the strain energy of the beam can be determined using Equation (2.4). For the case of a fixed-end beam, strain energy is as follows:

$$U(Q_1, Q_2, Q_3) = \frac{EA}{2S_0}\left(\frac{\pi^4}{256L^2}\right)\left[{Q_1}^2 - {Q_{1,0}}^2 + 4{Q_2}^2 - 4{Q_{2,0}}^2 + 9{Q_3}^2 - 9{Q_{3,0}}^2\right]^2 + \pi^4 EI\frac{(Q_1 + Q_{1,0})^2 + (4Q_2 + 4Q_{2,0})^2 + (9Q_3 + 9Q_{3,0})^2}{16L^3} \tag{2.13}$$

where S_0 is given in Equation (2.11). Using the imposed constraints, the strain energy is minimized for different values of δ (i.e., displacement controlled), and Q_1, Q_2, and Q_3 are determined for each value of δ. Past studies often do not include the effects of axial strain on the total strain energy in the beam (Harvey and Virgin, 2015), as the beams were taken to be incompressible. This results in the coefficients Q_n being quadratic in the equation for strain energy, and thus being relatively simple to solve. For the case of this study, where axial strain is being considered in the total strain energy, the coefficients Q_n are 4th order, resulting in the need to use a numerical solution to solve the problem rather than an analytical solution. Additionally, the forces required to generate the shape function based off of the undeformed shape is given by λ. Using these values, a force-displacement curve is able to be determined for different shapes of beams.

2.2.3 Input Parameters

The energy minimization model is input into MATLAB. This allows for it to be solved numerically, as the problem ends up becoming a nonlinear minimization due to the

terms for axial strain. To do this, two thousand δ values are taken, ranging from $\delta = 0$ to $\delta = 2H$. The equation for U is input based off of the initial conditions that are entered into MATLAB, leaving Q_1, Q_2, and Q_3 as variables that need to be determined. Afterwards, the constraint equation is determined by taking the displacement of the beam at $x = L$ ($y(L)$) and subtracting the initial rise minus the displacement, $H - \delta$, which is multiplied by a Lagrange multiplier, λ, which represented the amount of force needed to generate a given δ. This is then added to $y(x)$ (Equation 2.7), a function of Q_1, Q_2, Q_3, x, and L, to become the constraint function. To solve for λ, Q_1, Q_2, and Q_3, the MATLAB function *fmincon* is used to determine the minimum value of the strain energy equation, U, subjecting it to the constraint equation. This then allows for MATLAB to numerically determine each of these values for different values of δ. From these results, the amount of force required to generate a given displacement and the shape of the beam for each displacement is able to be determined.

Using the energy minimization model, several different parameters are able to be adjusted. The length (L) of the beam is taken to be 92.08 mm. For the polylactic acid (PLA) the beams are made out of, the Young's modulus (E) is taken from the technical data sheet from the manufacturer (Polymaker, 2017). The value the model uses is 2,636 MPa. However, there is a variance of 330 MPa in the material, according to the technical data sheet (Polymaker, 2017). This represents a large variance (12.5%) when compared to the initial value, meaning that the beams' actual Young's modulus likely varies from what is used in the model. The width and thickness of the beam are taken to be 25.4 mm and 1.59 mm, respectively. Therefore, the flexural rigidity (EI) and axial rigidity (EA) are found to be 0.022 N·m^2 and 1.06×10^5 N, respectively. The rise (H) of the beam is taken to be 19.05 mm in order to correspond with the physical prototype of the system discussed in this research (Chapter 3).

One parameter that is adjusted between tests is the seeding of different mode shapes

into the initial beam, $Q_{1,0}$, $Q_{2,0}$, and $Q_{3,0}$. Coefficient $Q_{1,0}$ is the most dominant mode shape in the beam that is considered in Chapters 3 and 4, as $Q_{1,0}$ results in the negative stiffness in the beam. All three parameters are adjusted in this model in order to investigate the effects of different mode shapes. Specifically, all three parameters are adjusted in terms of the nondimensional initial Fourier coefficients q_n, where $q_n \equiv Q_{n,0}/H$.

Theoretically, the geometry of the beam could be adjusted in order to affect the relationship between strain energy due to bending and strain energy due to axial deformation. However, in the case of this research, a rectangular beam cross section is assumed for all tested cases.

2.2.4 Energy Minimization Results

Several different methods are used for viewing the results of the energy minimization model.

One analysis MATLAB performs on the energy minimization model results is looking at the deflected shape of the beam at different end-displacements (δ) imposed on the beam. This allows for the progression of the beam's shape as end-displacement is applied to be graphically displayed. Along with this, a force-displacement curve for each beam is created, so as to allow for the deflected shapes to be easily compared to a location along the force-displacement curve. Results for the beam shapes and force-displacement curves from the energy minimization model are provided in Figure 2.3 for the case of $q_1 = 1.00$, $q_2 = -0.01$, and $q_3 \approx 0$ using only one beam. For this figure and all of the other results figures in this chapter, beam shapes are shown in a variety of different colors as increasing displacement is applied to the system. These beam shapes correspond to different colored points along the force-displacement curve, which can be used to indicate how much force is required for a given beam shape. This allows for the progression of beam shape to be easily compared to the force-displacement curve.

For the actual design of the quasi-zero stiffness isolation system in practice, two

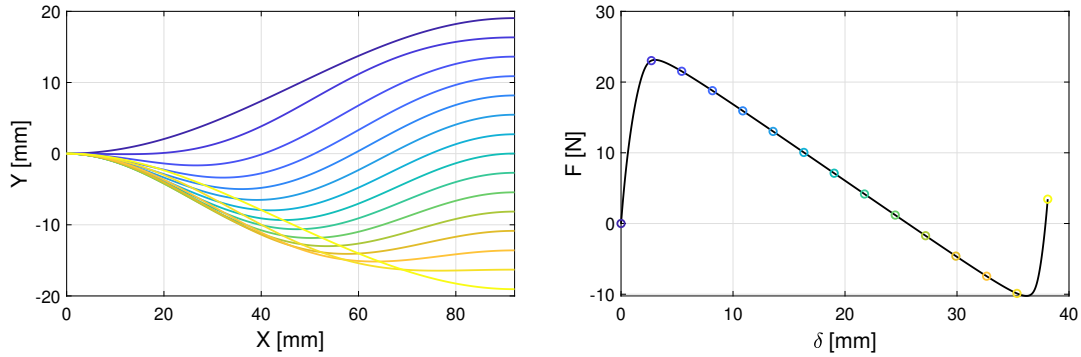

Figure 2.3: Theoretical displacement history (left) and force-displacement curve (right) for a single design beam using the energy minimization model: $q_1 = 1.00$, $q_2 = -0.01$, and $q_3 \approx 0$.

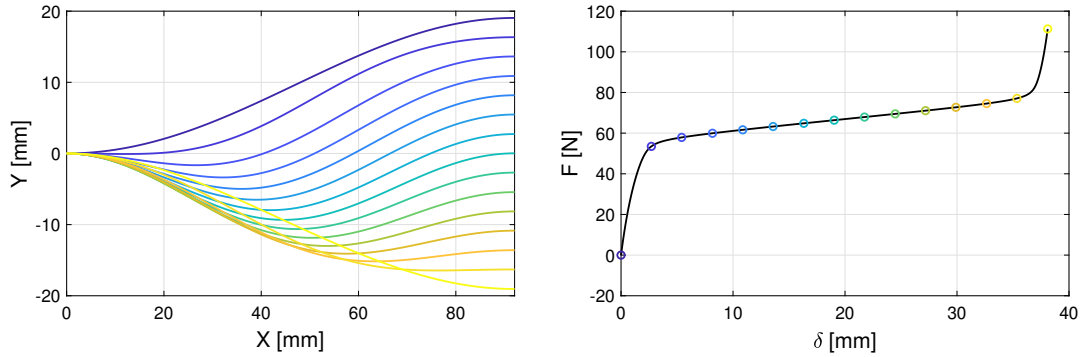

Figure 2.4: Theoretical displacement history (left) and force-displacement curve (right) for the quasi-zero stiffness isolation system—two design beams and a spring—using the energy minimization model and $q_1 = 1.00$, $q_2 = -0.01$, and $q_3 \approx 0$.

beams are used in order to create a symmetrical system. Because of this, the energy stored by the beams for a given displacement is taken as double, as both halves of the beam are intended to have the same parameters. As a result, the stiffness of the beams is taken as double that of what it would be with one beam. Additionally, a spring is used in parallel with the beams. The stiffness of the spring is taken to be 2.74 N/mm.

Comparing the previous result, for that of a single beam (Figure 2.3), to that of the system in practice, with two beams and a spring (Figure 2.4), yields different results. Results for the beam shapes and force-displacement curves from the energy minimization model are provided in Figure 2.4 for the case of $q_1 = 1.00$, $q_2 = -0.01$, and $q_3 \approx 0$ with two beams and a spring.

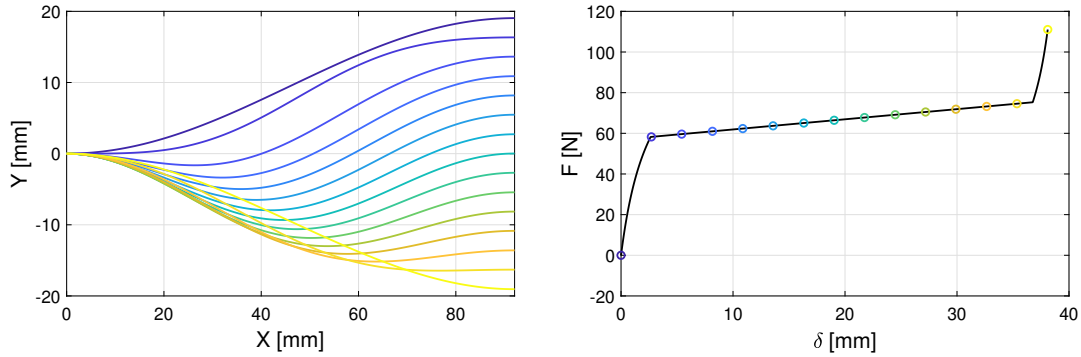

Figure 2.5: Theoretical displacement history (left) and force-displacement curve (right) for the quasi-zero stiffness isolation system—two design beams and a spring—using the energy minimization model: $q_1 = 1.00$, $q_2 = -10^{-8}$, and $q_3 \approx 0$.

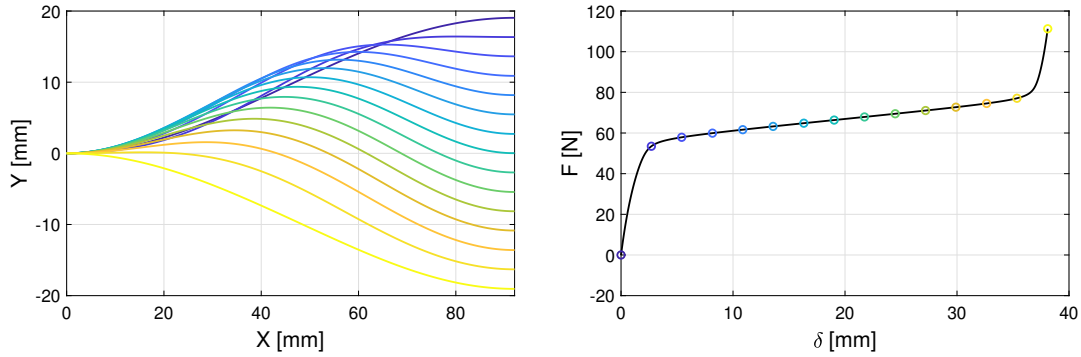

Figure 2.6: Theoretical displacement history (left) and force-displacement curve (right) for the quasi-zero stiffness isolation system—two design beams and a spring—using the energy minimization model: $q_1 = 1.00$, $q_2 = 0.01$, and $q_3 \approx 0$.

Adjusting q_2 has the effect of changing how dramatically the beam's stiffness changed. Lower values of q_2 result in sharper angles (or "knees") in the force-displacement curve, whereas larger values of q_2 result in a smoother curve. For example, the force-displacement curve shown in Figure 2.5 ($q_2 = -10^{-8}$) has sharper angles than that shown in Figure 2.4 ($q_2 = -0.01$). Using a positive value for q_2 has the result of significantly changing the path the beam takes as it is displaced. This can be seen in Figure 2.6 ($q_2 = 0.01$).

Adjusting q_3 has interesting effects on the shape of the force-displacement curve for the beam. Both q_1 and q_3 have effects on the amount of rise in the beam, and thus for this particular model have to add up to 1 in order to satisfy $y_0(x = L) = H$. q_1 has

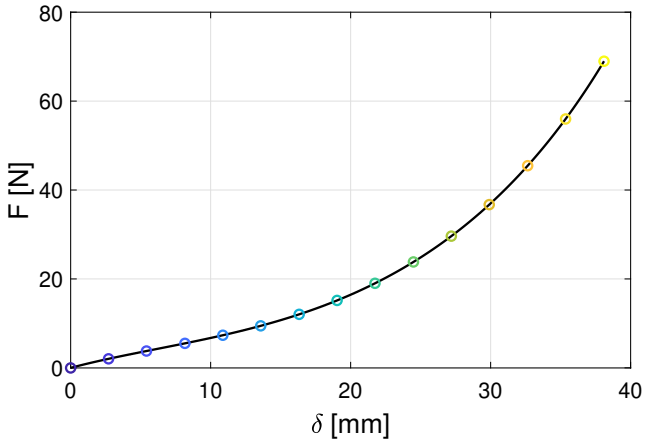

Figure 2.7: Theoretical force-displacement curve for the design beam using the energy minimization model: $q_1 = 0.25$, $q_2 = -0.01$, and $q_3 = 0.75$. No spring is included in this force-displacement curve.

the effect of creating an initial positive stiffness, followed by a negative stiffness for a period, as the beam is snapping-through, with the stiffness eventually changing back to positive. q_3 has the effect of starting off with a low stiffness that greatly increased with force. This effect can be seen in Figure 2.7. Additional discussion on this can be found in Appendix B.

For the design beam as it appears in Chapter 3, stiffnesses can be taken from the force-displacement curve for both the design beam and the combined system consisting of both the beam and the spring. These results can later be used to verify the results of the static testing. Results for stiffnesses are provided in Figure 2.8. The negative stiffness of the beam and the positive stiffness of the combined system are found to be -2.17 N/mm and 0.57 N/mm, respectively. Hence, the positive stiffness spring is counteracting the negative stiffness of the beams to produce a low stiffness, which is desirable for isolation. The quasi-zero stiffness system settles around 20 mm for a 62-N isolated weight. For a linear spring with the same operating stiffness (0.57 N/mm), the static displacement would be 108.8 mm. Therefore, the initial, high positive stiffness prior to the quasi-zero stiffness greatly reduces the static settlement in the isolation

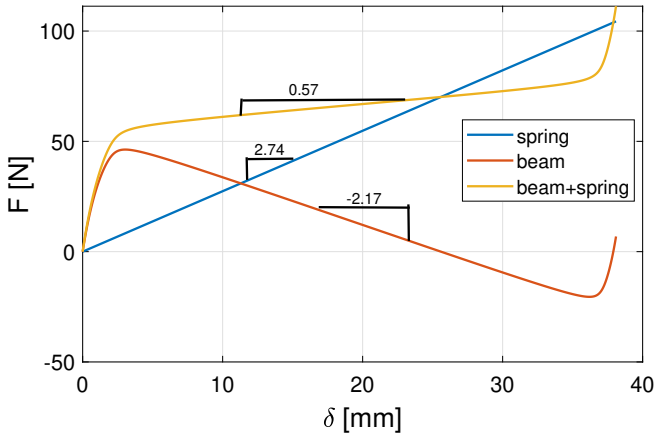

Figure 2.8: Theoretical force-displacement curve for the quasi-zero stiffness isolation system—two design beams and a spring—using the energy minimization model: $q_1 = 1.00, q_2 = -0.01$, and $q_3 \approx 0$.

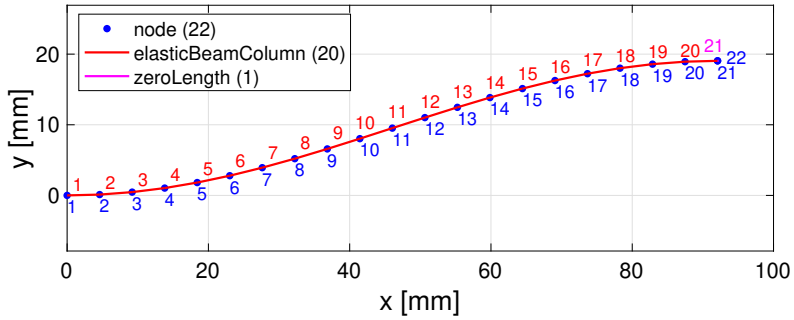

Figure 2.9: Node and element layout for the OpenSees model.

system under gravity loads (self weight). This is the same concept that is behind the "high static low dynamic stiffness" vibration isolators proposed by others (Shaw et al., 2013).

2.3 OpenSees Model

The second method that is used to evaluate the isolation system is an OpenSees finite element model.

2.3.1 Input Parameters

To begin, properties of the design beam used in the dynamic testing are inputted into a tool command language (TCL) file (see Appendix C), in order to allow for OpenSees to

read the file. Twenty-one different nodes are used at equal points along the horizontal length of the beam, as shown in Figure 2.9. These nodes consist of their location along the length of the beam as their x-coordinate and their vertical offset from the centerline of the supports as their y-coordinate. Additionally, a 22nd node is used with the same coordinates as the inside end condition (node 21), which allows for the setup to maintain the fixed end condition on the inside while still translating vertically. Node locations are assigned by taking a first beam deflection shape $\psi_1(x)$ with a rise of 19.05 mm and a length of 92.08 mm, to match the experimental system (Chapter 3). Following that, a small amount of second shape $\psi_2(x)$, varying between tests, is added to each beam shape. These imperfections help to smooth over the force-displacement curves, as will be discussed later in Section 2.3.2. After describing the different nodes used in the model, boundary conditions for each node are prescribed. Nodes 1 (outer end) and 22 (inner end) are both completely fixed, while node 21 (inner end) is allowed to translate in the y-direction. In the above definition, "outer end" corresponds to the fixed condition on the left side, and "inner end" corresponds to the fixed connection on the right side that is allowed to translate in the y-direction, as is represented in Figure 2.1. This allows OpenSees to view the beam as it would move in practice.

Following prescribing the boundary conditions, section properties are set. As is the case in Section 2.2, PLA is used as the material for the beam, so the Young's modulus is taken to be 2,636 MPa. The area is taken to be 40.323 mm^2, and the second moment of area is taken to be 8.468 mm^4, both of which represent the design beam as it is drawn, but as is mentioned in Chapter 3 does not accurately represent the beam due to difficulties in the printer accurately printing the beam. As a result, the OpenSees model ends up using an area and a second moment of area that both under represent that of the design beam.

After the section properties are set, elements are defined between each node. Each

element except for the element connecting nodes 21 and 22 is set as an *elasticBeamColumn*, using the previously mentioned section properties and a *corotational* coordinate transformation. The element between nodes 21 and 22 was defined as a *zeroLength* element, with elastic uniaxial material properties, namely a stiffness of 2.74 N/mm. This positive stiffness element, which represents the spring, also acts as regularization to avoid negative stiffnesses in the finite element model.

2.3.2 OpenSees Results

In order to obtain results, a series of increasing vertical displacements are applied to the beam at node 21. OpenSees then performs a finite element analysis on the system in order to determine forces and displacements at each specified node for each prescribed displacement. Node displacements and forces are recorded and outputted for each result. These results are then imported into MATLAB so that they can be analyzed. Several different analyses are done on the results for the different trials.

One analysis MATLAB performs on the OpenSees results is through looking at the deflected shape of the beam at different loads applied to the beam. This allows for the progression of the beam's shape as load is applied to be graphically displayed. Along with this, a force-displacement curve for each beam is created, so as to allow for the deflected shapes to be easily compared to a location along the force-displacement curve. Results for the beam shapes and force-displacement curves from the OpenSees model are provided in Figure 2.10.

As discussed in Section 2.2, adjusting the amount of second mode buckling, q_2 seeded into the shape of the beam results in changes to the second Fourier coefficient for the shape of the beam, Q_2, and the shape of the force-displacement curve. Seeding in a larger amount of second mode buckling results in smoother force-displacement curve. The Fourier coefficient for third mode buckling, Q_3, is not considered in the OpenSees model, nor is third mode buckling, q_3, seeded into the design of the beam. Results for

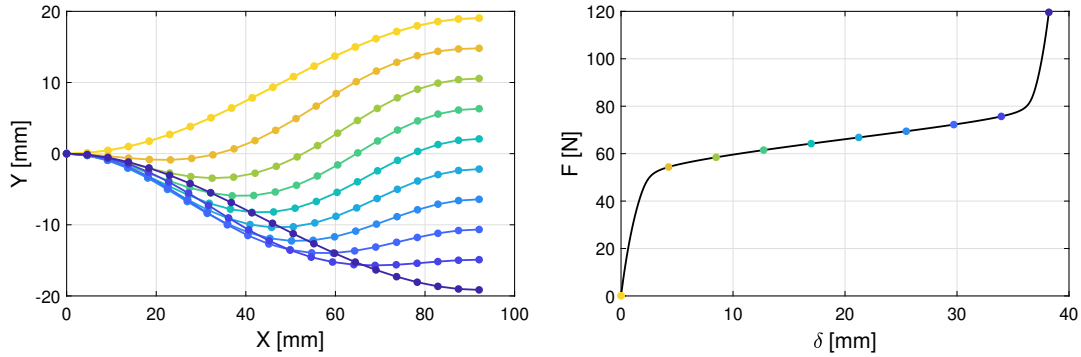

Figure 2.10: Theoretical displacement history (left) and force-displacement curve (right) for the quasi-zero stiffness isolation system—two design beams and a spring—using OpenSees: $q_1 = 1$, $q_2 = -0.01$, and $q_3 = 0$.

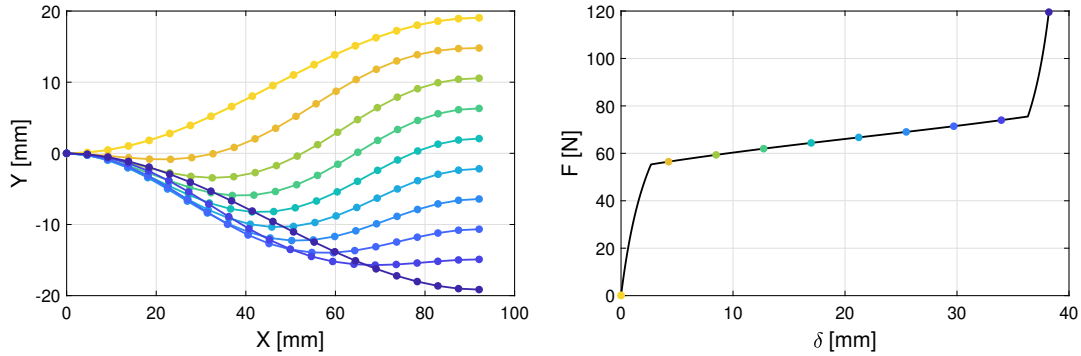

Figure 2.11: Theoretical displacement history (left) and force-displacement curve (right) for the quasi-zero stiffness isolation system—two design beams and a spring—using OpenSees: $q_1 = 1$, $q_2 = -10^{-8}$, and $q_3 = 0$.

the beam shapes and force-displacement curves from the OpenSees model are provided in Figure 2.11.

The beam shapes can be broken down at different amounts of loading into first mode and second mode buckling, represented by Q_1 and Q_2 respectively. This is done through using Fourier coefficients, similarly to how they are used for initially seeding the shape of the beam. These results are provided in Figures 2.12 and 2.13 for $q_2 = -0.01$ and -10^{-8}, respectively.

As could also be seen in the force-displacement curves for the beams, seeding in a larger q_2 value results in smoother curves, as the beam less dramatically shifts from being in first mode to second mode. These results show that even slight changes to the

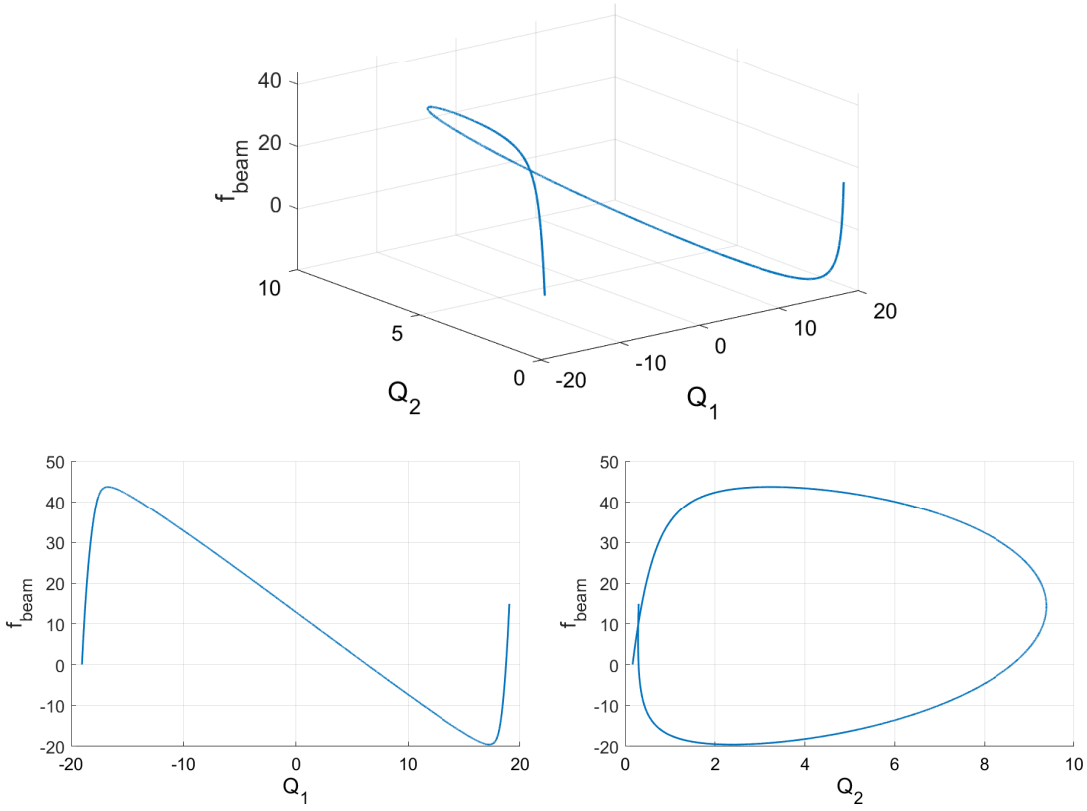

Figure 2.12: Force [N] versus Fourier coefficients [mm] from OpenSees model: $q_1 = 1$, $q_2 = -0.01$, and $q_3 = 0$.

shape of the beam result in significant differences in beam performance.

Finally, the force-displacement curve for the setup is looked at to determine the impact of the spring on the setup. In order to do this, the effects of the spring are subtracted out from the effects of the combined system, as OpenSees needs the structure to have a positive stiffness in order to solve the system. This is simple to do, as the spring possesses a constant stiffness, meaning that the force-displacement relationship of the spring is linear. To obtain the force-displacement curve of only the beam, the linear force-displacement of the spring is subtracted from that of the combined system, and the results are graphed. These results for $q_2 = -0.01$ are provided in Figure 2.14. From the OpenSees model, it is determined that the beam has a negative stiffness of 2.09 N/mm as it is snapping through, and when combined with the spring has a positive

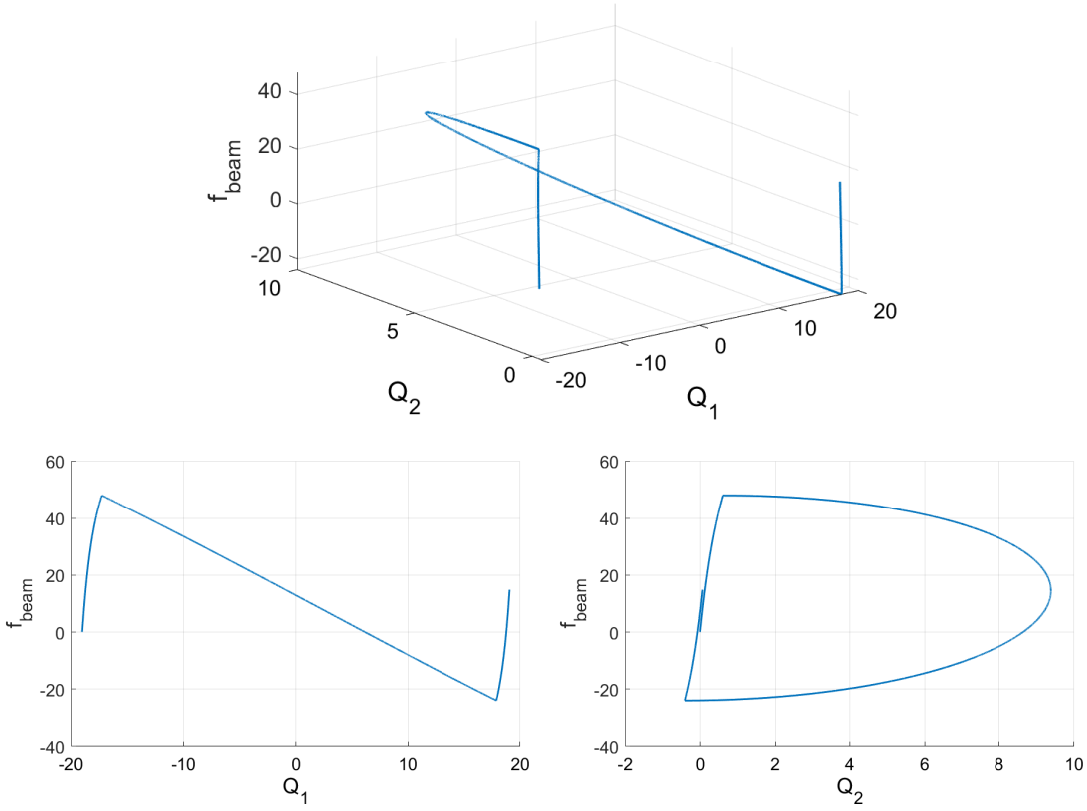

Figure 2.13: Force [N] versus Fourier coefficients [mm] from OpenSees model: $q_1 = 1$, $q_2 = -10^{-8}$, and $q_3 = 0$.

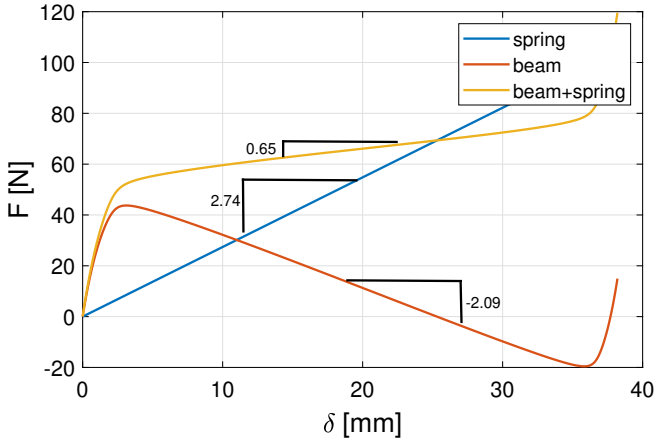

Figure 2.14: Theoretical force-displacement curve for the design beam, design spring, and combined setup using OpenSees: $q_1 = 1$, $q_2 = -0.01$, and $q_3 = 0$.

stiffness of 0.65 N/mm while snapping through. These results are in good agreement with the energy minimization approach (Figure 2.8).

2.4 Summary

Two different methods are used for theoretically determining the stiffnesses of the beam and of the combined system. The first method used is an energy minimization model, which seeks to find deflected shapes of the beam through minimizing the energy stored in the beam based off of its deflected shape using Fourier coefficients. From the energy minimization model, it is determined that the negative stiffness of the beam is -2.17 N/mm and the positive stiffness of the combined system is 0.57 N/mm. The second method used is a numerical method using a platform known as OpenSees to simulate loading on the beam and determine displacements and forces within the beam. From the OpenSees model, it is determined that the negative stiffness of the beam is -2.09 N/mm and the positive stiffness of the combined system is 0.65 N/mm. These results show that the models are consistent with one another. In Chapter 3, the experimental results of the static testing are determined and are compared to the results from the theoretical models discussed in this chapter.

Chapter 3
Characterization Tests

3.1 Overview

In this chapter the system design is discussed and the static testing results are analyzed for the finalized system. Results from previous experiments for this test setup can be found in Appendix A. The results from the static testing are then used to design an acceptable configuration for the final setup for the dynamic testing and to determine a design loading for the dynamic testing. Static testing consists of testing printed beams on an Instron machine, which measures the amount of force needed to create a given deflection. This can then be used to characterize each beam and create force-displacement curves, from which stiffness can be extracted.

3.2 System Setup and Design

3.2.1 Design Parameters

The characterization tests span over several iterations of the design in order to further improve the design while still gaining understanding about the working of the system. Previous iterations consist of different beam shapes and spring arrangements. Information on those designs and tests can be found in Appendix A. Following the completion of those tests, a series of significant redesigns is performed on the system, which aims to address many of the shortcomings of the initial design. The redesigned experimental setup, incorporating the modifications discussed below, is shown in Figure 3.1

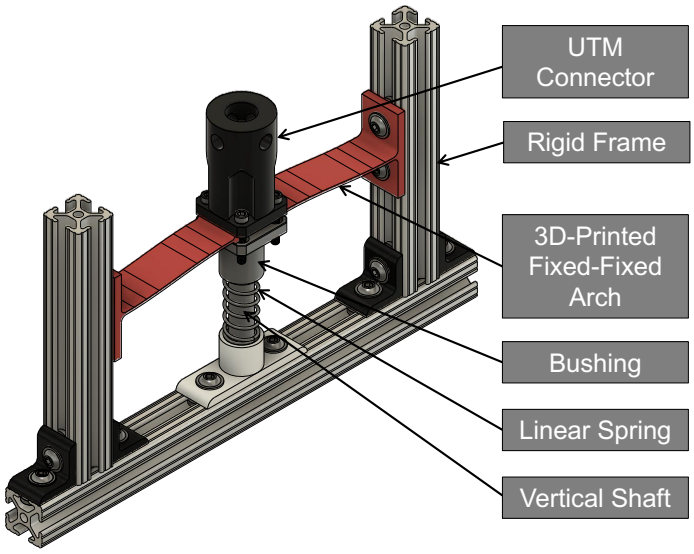

Figure 3.1: CAD model of the experimental setup design incorporating modifications based on previous designs.

Firstly, a vertical shaft is added in order to help improve the stability of the system. This allows the center of the beam to be tracked along the rail through the combination of the shaft and a bushing. As a result of this change, a fixed connection along the center of the beam is also used in order to fix the beam to the bushing. A new universal testing machine (UTM) connector is designed in conjunction with the bushing in order to provide the fixed connection while maintaining the connection to the Instron testing machine (Figure 3.2). In addition to improving the stability of the system, the vertical shaft also allows for a spring to be placed directly on the shaft, greatly simplifying the design.

For the final design, the beam uses fixed connections for both the ends of the beam and for the loading mechanism. The fixed conditions for the ends of the beam involve printing the bolt holes directly onto the beam, which allows the beam to be directly mounted to the rails. The fixed condition for the loading mechanism involves bolting the UTM connector and the bushing to the center of the beam. These fixed connections helps reduce the variability in the system, as the old system struggles with the beam

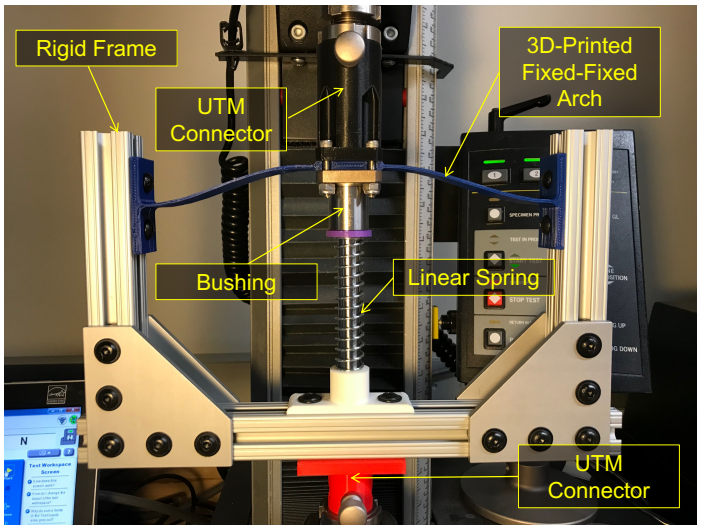

Figure 3.2: Experimental setup in the Instron load frame.

sliding around in the pinned connections. Additionally, it changes the deflected shape of the beam so that it represents a full sine wave instead of half a sine wave. This then affects the amount of energy stored in the beam, as is covered in Chapter 2. The beams are also printed such that they have an initial camber. The final camber in the design beam was selected to be 19.05 mm (0.75 in.), which is used in the analyses in Chapter 2; however, several different cambers are seeded, printed, and tested. The initial camber in the beam has an advantage in that it allows for the beam to be unstressed when unloaded, preventing plastic deformation from occurring when the beam is not being tested. Another consideration for the beams is to separate the left and right halves of the beam in order to allow for variation with regards to thickness on different halves. This idea is eventually discarded due to it amplifying the effects of asymmetries. However, with a more precise system the results could prove more effective.

Parameters which vary in the beam include length and rise. After experimentation with the test setup, it is determined that length needed to become a fixed parameter and only rise would vary between controlled tests. This is due to the difficulty with which a good alignment of the test setup is to attain. Extreme precision is needed in order to

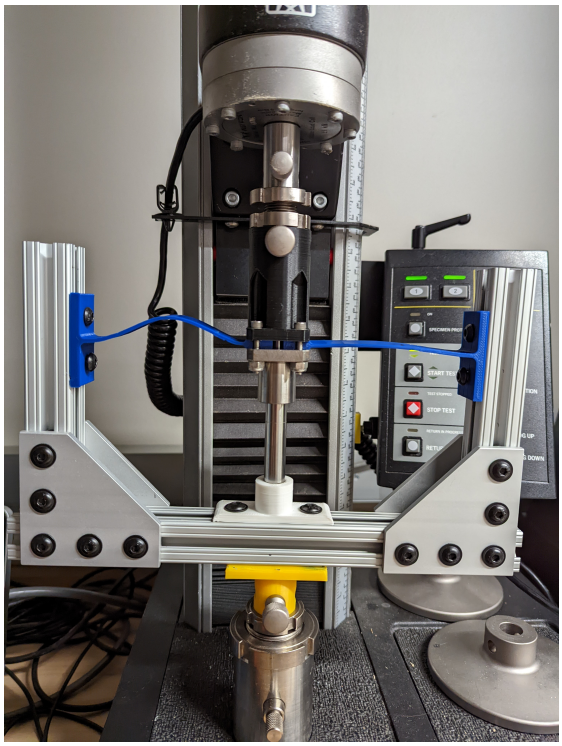

Figure 3.3: A small asymmetry causes large differences in the rises and thus the stresses experienced between the sides of the beam.

minimize asymmetries with the setup. Examples of the effects of small asymmetries can be seen in Figure 3.3. Asymmetries also result in large forces in the connections within the system. Moving the rails that the beam is mounted to results in a difficult alignment being needed between every variance with regard to length. Furthermore, minute changes result in different amounts of axial shortening, and thus different axial loads being experienced by the beam, changing the energy imparted into the beam and the results of the force-displacement curve. Because of this, length is removed as a consideration for this particular test setup. A fixed length of 228.60 mm (9 in.) is used for all beams printed from this point forward, allowing for a utilization of most of the length of the base of the setup.

Rise is initially seeded into every single beam printed following the redesign of the test setup. Figure 3.4 shows an example beam, with the rise being the distance between the two centerlines spanning horizontally across the page. The rise used for

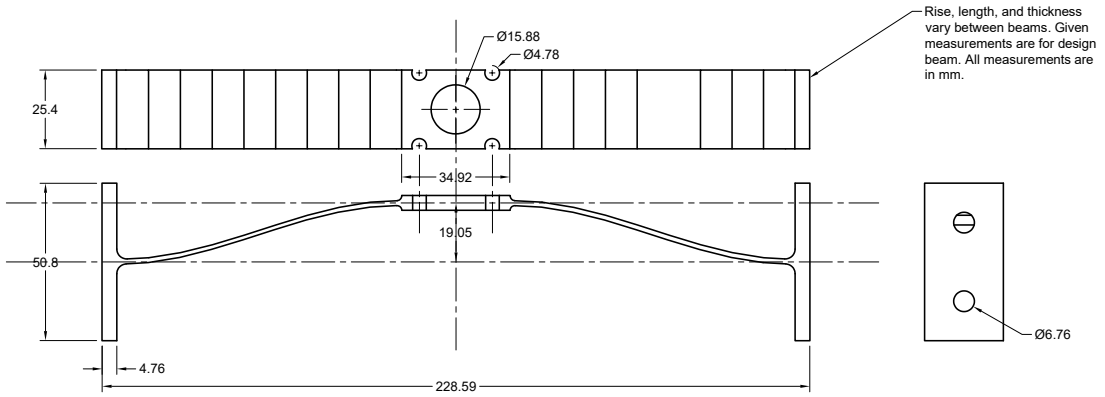

Figure 3.4: A drawing of the design beam used for the final design of the beam. The rise for this beam is 19.05 mm.

the setup is intended to be reflected using the shape of a sinusoidal function, as that is the buckled shape of a beam with fixed ends that are free to translate vertically. Rises of 12.70 mm (0.5 in.), 19.05 mm (0.75 in.), and 22.23 mm (0.875 in.) are considered in this research. Choosing beams with larger rises is advantageous because it allows for larger ranges of deflections to be applied to the setup due to the larger height with which the beam would be snapping through if not constrained. However, too large of a rise results in not being able to use the entire operating range due to the spring fully compressing. Additionally, larger rises result in higher negative stiffnesses exhibited by the beams. As was mentioned earlier, a rise of 19.05 mm is used for the final beam selection. This allows for the entire operating range of the beam to be utilized without fully compressing the spring.

The final parameter considered in this experiment is the thickness of the beam. The thickness of the beam is important in that it changes the section properties of the beam significantly. This is due to thickness having a cubic effect on the second moment of area of a beam. Although thickness is the parameter which is most free to change, it is constrained by the number of layers the 3D printer is able to use. More mention of this and other 3D printer properties are given in Section 3.2.2. Several different thicknesses

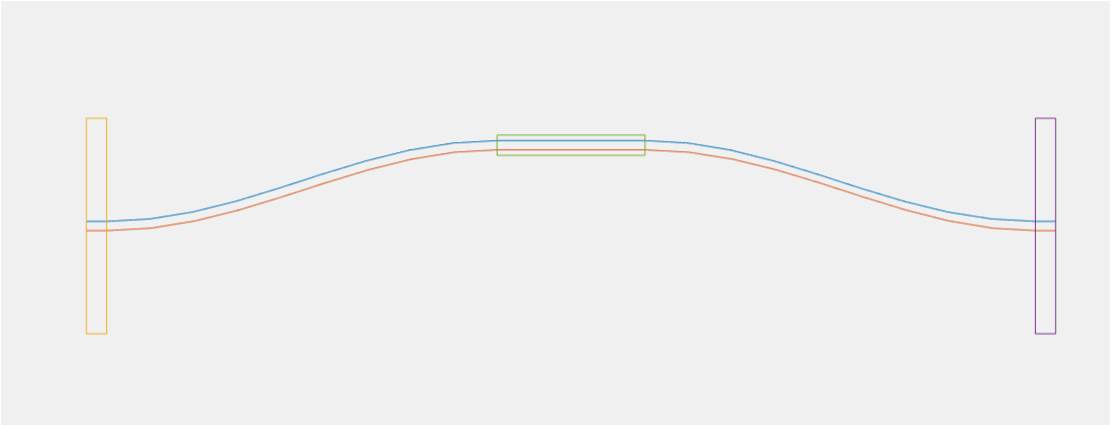

Figure 3.5: An example of the beam cross section that MATLAB outputs before it is extruded in Fusion 360.

are considered including 0.99 mm (5/128 in.), 1.39 mm (7/128 in.), 1.59 mm (1/16 in.), 1.79 mm (9/128 in.), and 2.18 mm (11/128 in.), but due to the 3D printer nozzle being a certain width the 1.39 mm and 1.79 mm are discarded due to being too similar to the 1.59 mm thick beam. Since the 1.59 mm thick beam has ideal results when paired with the other parameters, it is selected for the final beam design.

3.2.2 Computer-Aided Design and 3D Printing

To create the beams, 3D models of the beam need to be created in order to print them. A MATLAB code is used in order to take given dimensions and generate a .svg figure that could then be turned into a .stl file using Fusion 360. Results from the MATLAB code can be seen in Figure 3.5. An example of a beam drawn in Fusion 360 can be seen in Figure 3.6. Using MATLAB and Fusion 360 in conjunction, beams are able to be drawn up and printed very quickly and formulaically, allowing for rapid variation between tests.

For the final beam design, four different beams are printed, taking care to make sure they are printed in the exact same manner in order to ensure that each beam would be the same. Beams are sliced using Cura LulzBot Edition 3.6.29 software and printed on a LulzBot TAZ6. All beams are printed on their side in order to remove the need for

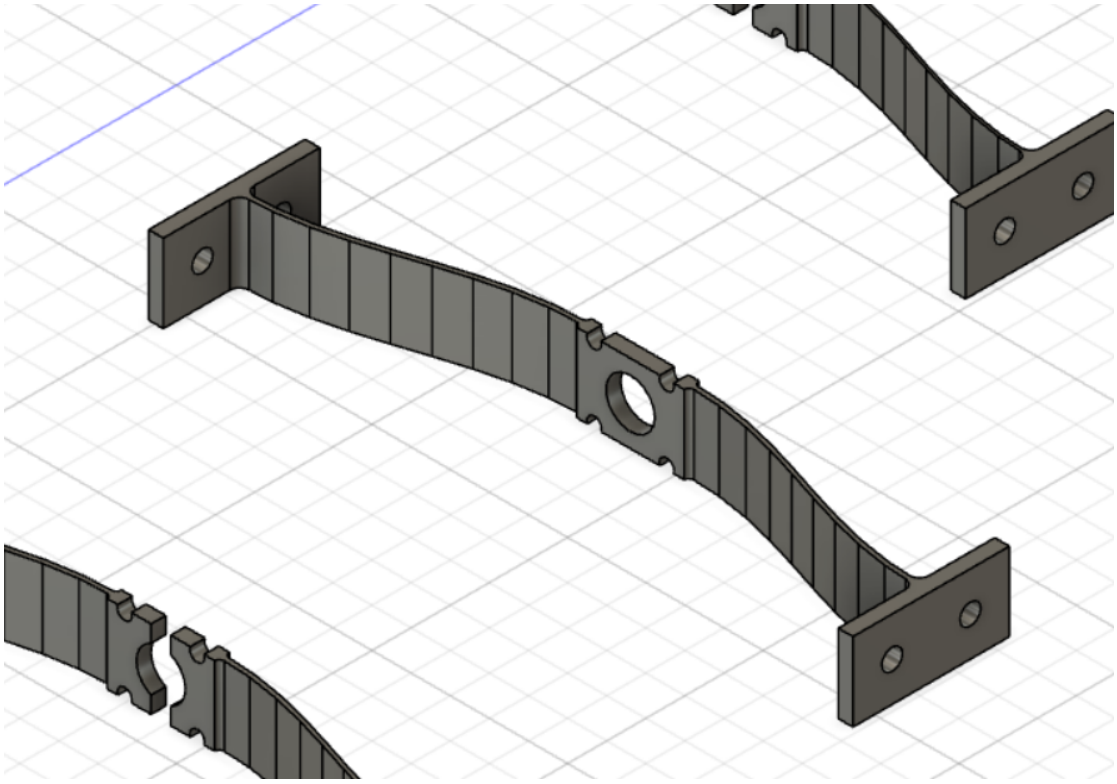

Figure 3.6: One of the beams tested and printed drawn in Fusion 360.

support material while printing. This also has the benefit of allowing smoother profile lines over the course of the curves as it is printing. Measures taken include using the same .stl file, cleaning off the bed prior to each print with acetone, and using the same filament for every print. Beams are printed using PolyLite PLA in high detail mode, with a filament profile of 0.180 mm and 100% infill (Polymaker, 2017). No supports are used on the setup while printing.

At one point, while placing the setup in the Instron machine, the 3D printed plastic UTM connector snapped at the pinned connection. An image of the broken UTM connector can be seen in Figure 3.7. Following this, the 3D printed UTM connector was created using 100% infill as well. No other parts had to be reprinted after this; however, none of the other 3D printed parts were likely to have significant stresses, so the printer properties for these parts would not matter for the function of the system.

Figure 3.7: The UTM connector for the system snapped off while attaching the setup to the Instron machine.

All other printer settings are left at the default settings for the given material for the given software version and printer. As was mentioned in Section 3.2.1, certain beam parameters were based off of the printer settings. Using a different 3D printer, slicing software, or filament would likely result in slightly different beam performance.

3.2.3 Variation in 3D-Printed Beam Geometry

After the beams are all printed but prior to testing, measurements for thickness and width are taken for each beam using calipers at 6 different locations along the length of the beams. These measurements are recorded and compared to one another in order to determine how similar the beams are to one another before plastic deformation from testing occurs. Previous prints and measurements indicated that the printer is inconsistent with printing the beams symmetrically. Results from the measurements confirm these suspicions. The 4 beams have a standard deviation ranging between 0.02 mm and

0.2 mm for thickness and width, with similar variation for both thickness and width. However, the variation in the thickness is more significant than the variation in the width due to the variation making up a larger proportion of the total value. In fact, the variation in the thickness makes up as much as 7 percent of the thickness of the beam. It is also found that the beams have more variation closer to the center of the beam than at the edges of the beam as a result of printing. Additionally, it is noted that the left sides of the beams are consistently thicker than the right sides of the beams. This contributes to a larger moment of inertia in the left sides of the beams, and thus a difference in the energy states that the beams can store between sides. It is unknown why either of those would be the case. The results for measured values of the beams are provided in Table 3.1.

The beams measured values are compared against one another and the most average beam, Beam 1, was set aside for dynamic testing. This allows for Beam 1 to be fresh and untested with no plastic deformation prior to dynamic testing. This also helps to ensure that the results for dynamic testing is able to be explained by the static testing results, as the static testing results discussed in this chapter are also for virgin beams.

Table 3.1: Measurements [mm] of the beams used for static and dynamic testing. Darker shading indicates higher coefficients of variation. Beams 2, 3, and 4 are used for static testing. Beam 1 is used for dynamic testing.

Location	Thickness (T) or Width (W)	Beam 1	Beam 2	Beam 3	Beam 4	Mean	Coefficient of Variation
10 mm	T	1.97	2.08	1.94	1.97	1.99	0.0268
10 mm	W	25.65	25.62	25.65	25.58	25.63	0.0011
50 mm	T	2.15	2.10	1.93	2.03	2.05	0.0402
50 mm	W	25.58	25.59	25.62	25.56	25.59	0.0008
90 mm	T	2.44	2.36	2.23	2.02	2.26	0.0702
90 mm	W	25.34	25.09	25.55	25.51	25.37	0.0071
140 mm	T	2.19	2.16	1.90	1.89	2.04	0.0690
140 mm	W	25.38	25.22	25.54	25.57	25.43	0.0055
180 mm	T	1.72	1.70	1.61	1.52	1.64	0.0485
180 mm	W	25.56	25.39	25.65	25.54	25.54	0.0037
220 mm	T	1.90	1.78	1.76	1.79	1.81	0.0301
220 mm	W	25.66	25.66	25.71	25.50	25.63	0.0031

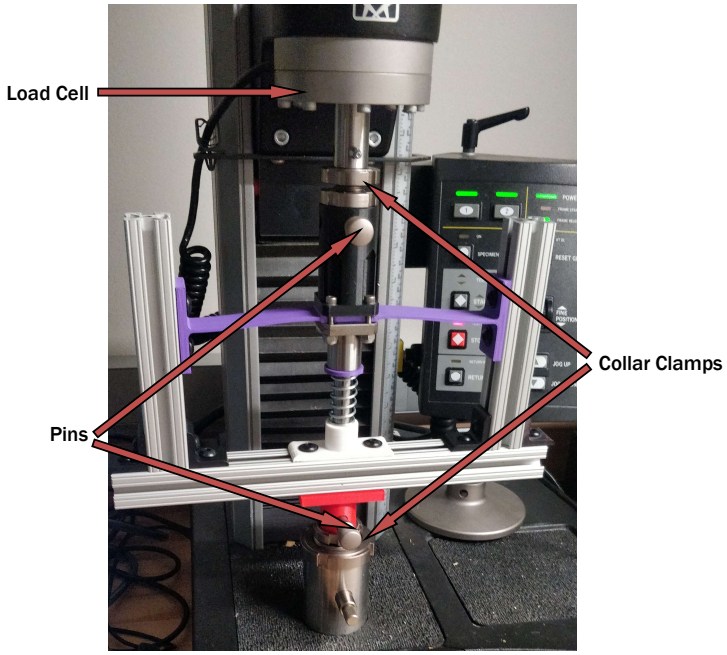

Figure 3.8: Test setup as it is placed in the Instron testing machine.

3.3 Static Testing Results

Following the completion of measurements, Beams 2, 3, and 4 are statically tested using the Instron testing machine mentioned in Appendix A. This test setup can be seen in Figures 3.2 and 3.8.

Each beam is tested twice, once going over larger displacement ranges, and once oscillating about the expected operating range for the system. Each beam is loaded and unloaded such that they would produce a displacement at a rate of 25.4 mm/min. Every test is done in parallel with the chosen spring in order to reduce the effects of plastic deformation from repeated testing while most similarly replicating the way with dynamic testing is going to be performed. The force-displacement curve for the spring and for just the UTM connector are also obtained with the Instron machine in order to obtain the stiffness of the spring and the effects of friction respectively. These results

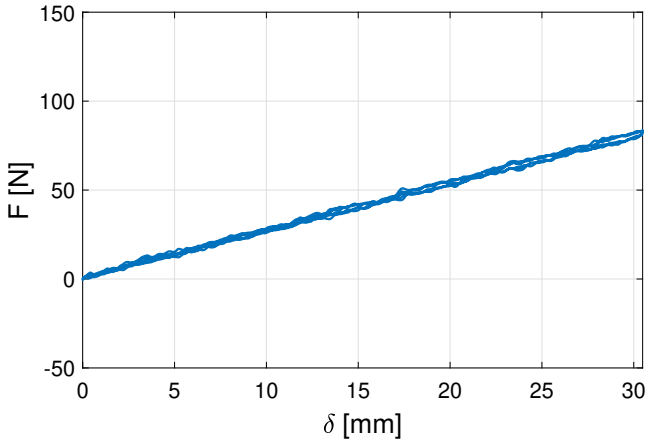

Figure 3.9: Measurements for the stiffness of the spring.

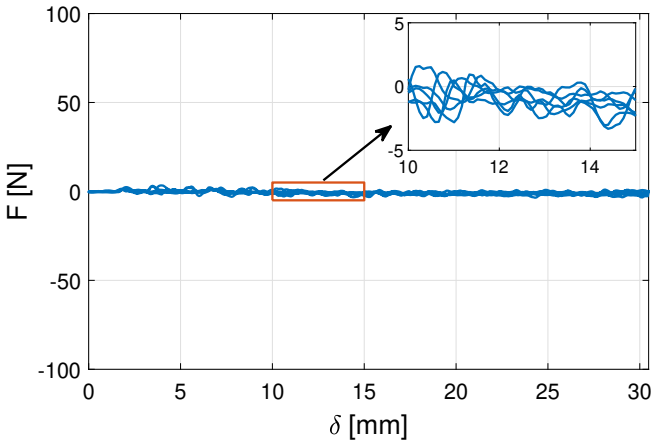

Figure 3.10: Measurements for the results of friction. Friction was found to have no noticeable impact on the system when compared to the stiffnesses contributed by the beam and spring.

are provided in Figures 3.9 and 3.10. The spring is found to have a stiffness of 2.74 N/mm whereas the friction is found to be negligible when compared to the stiffnesses of the spring and beams.

For Beam 2, testing is stopped midway through the first set of tests and the setup is slightly adjusted in order to reduce the effects of asymmetry. This results in some properties of the tests being slightly different than that of Beams 3 and 4. The results for the full cycle tests are provided in Figure 3.11.

Several important notes can be made using the results from the large range displace-

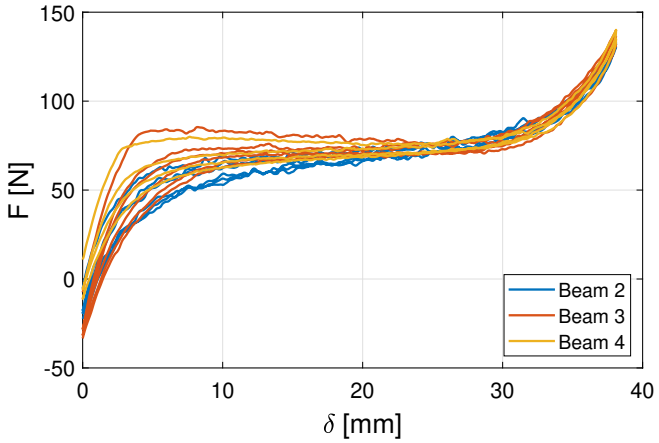

Figure 3.11: Measurements for the beams over a large range of displacement.

ment tests. Firstly, there is significant plastic deformation in the beams as they are being tested. For every trial, the initial loading follows a significantly higher path than the following loadings and unloadings. Energy is dissipated into the beam causing the plastic deformations, and this can be seen in the hysteresis between loading and unloading in the force-displacement curve. An example of the plastic deformation can be seen in Figure 3.12. Secondly, Beam 2 has a noticeably smaller drop-off on the first cycle than Beams 3 and 4, as a result of the test being restarted after the system was adjusted. This is also related to the plastic deformation in the beams, as Beam 2 had already experienced plastic deformation from being tested. In fact, Beam 4's plastic deformation following testing is compared to Beam 1's virgin state, and it is found that Beam 4 had an angle of 7.5° between fixed connections compared to 2.5° in Beam 1. Thirdly, the beams' operating ranges can be determined from the results of the large range displacement tests as the displacements which result in lower stiffnesses. From the results, the operating range is found to be roughly 8 mm to 30 mm.

For the oscillation tests, oscillation is performed between 10.16 mm (0.4 in.) and 25.40 mm (1.0 in.). The purpose of these tests is to get the stiffness of the beams when resisted by the springs over their operating range. Additionally, these tests are also used

Figure 3.12: An example of the plastic deformation experienced by the beams following static testing. These beams are lined up at the center. Pictured are beams 2 (bottom) and 3 (top).

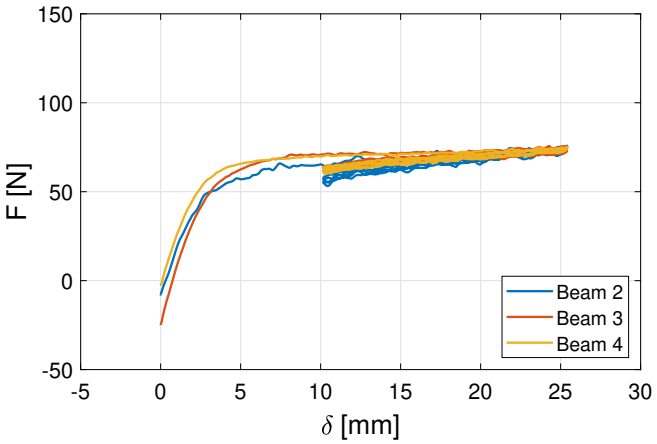

Figure 3.13: Measurements for the beams oscillating over a small range.

to ensure that the system's force-displacement curves act as expected over the course of several cycles. These results can be seen in Figure 3.13.

The results from the oscillation tests have to be corrected in order to have all results start at 0 mm rather than being based off of the initial force. As these tests are performed after the full-range tests, plastic deformation has already formed in the beams prior to the beginning of the oscillation tests. This causes the beams to start with a varying amount of negative force already applied, as the load head is pulling up on the beam. These forces are relatively large due to being located at a steep location on the stiffness curves of the beams. Once these negative forces are accounted for, it was found that all of the beams had the same operating load of roughly 69 N. The results for the oscillation

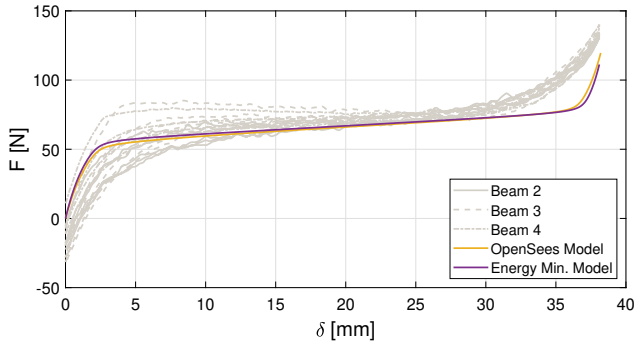

Figure 3.14: A comparison between the results of all of the models and prototype tests. Tests for theoretical models use $q_2 = -0.01$.

test can also be used to easily determine the stiffness of the systems. Beams 2, 3, and 4 are found to have average stiffnesses for their combined systems of 0.97, 0.55, and 0.63 N/mm, respectively. These correspond to negative stiffnesses of -1.77, -2.19, and -2.11 N/mm, respectively, after accounting for the 2.74 N/mm positive stiffness provided by the spring. It is expected for Beam 2 to have the largest stiffness as it has a larger second moment of area than Beams 3 and 4 (i.e., thicker, see Table 3.1). It is unclear why Beam 2 ended up having the lowest absolute value for negative stiffness. If Beam 1 were to be statically tested, it would be expected to have a stiffness most similar to that of Beam 2 due to it having a similar average second moment of area.

When comparing these results to the theoretical models discussed in Chapter 2, the stiffnesses of the beams from the prototype closely follow those determined using the models, as can be seen in Figure 3.14. It is found that the models more accurately represent the stiffnesses of the beams following plastic deformation occurring in the beams. Additionally, it is found that the models tend to represent a longer range over which softening occurs. Similarly, the theoretical models predict much sharper knees on the force-displacement curve than those which are determined experimentally.

3.4 Summary

The final beam used for the setup is 228.6 mm long, 1.588 mm thick, and with 19.050 mm rise. After removing fixed connections so that only sections of the beam in flexure are considered, each half of the beam is 92.08 mm long. There is found to be significant variation in thicknesses for the beams despite using the same printing setup for each beam, causing stiffnesses to vary a not insignificant amount from beam to beam. Despite the variation between beams, each combined setup exhibits a slightly positive, quasi-zero stiffness when statically tested. The average negative stiffness of the (2) beams is determined to be -2.02 N/mm, and the average stiffness of the combined setup is determined to be 0.72 N/mm. From static testing, it is found to have a significant softening over a displacement range between 10 and 30 mm as the beams are exhibiting negative stiffness. This is ideal behavior for the test setup leading into the dynamic testing in Chapter 4. Beams are found to have large plastic deformations as a result of the static testing. It is expected that as dynamic testing occurs, plastic deformation will occur, and thus the behavior of the setup will change.

Chapter 4
Dynamic Testing

4.1 Overview

Following the completion of static testing, dynamic testing is performed on the system in order to evaluate its performance. A virgin beam (Beam 1) is used in order to ensure that the plastic deformations Chapter 3 notes would not be present during the initial set of tests. In order to perform the dynamic testing, the test setup is attached to a vertical shake table so that different ground accelerations could be applied to the system. Tests performed on the system include harmonic tests, where the system is subjected to accelerations varying in a sinusoidal pattern at a given frequency, and white noise tests, where the system is subjected to a wide variety of frequencies and accelerations. The dynamic test results consist of measuring acceleration of the base and of the isolated mass at the top of the system to assess the transmissibility.

4.2 System Setup

Since dynamic testing is the final aim of this research, the system is setup with dynamic testing in mind over the course of the design. A three-dimensional shake table in Fears Structural Engineering Laboratory is used to perform the dynamic tests. The only two changes that needed to be made for the setup were to provide a method for attaching the setup to the shake table and to attach the mass to the setup.

In order to attach the setup to the shake table, the UTM (Universal Testing Machine)

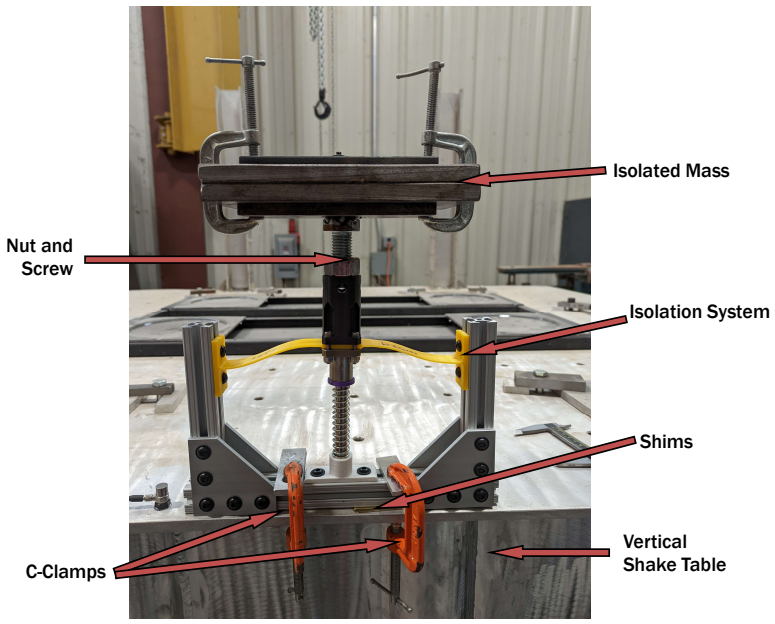

Figure 4.1: The setup after it is attached to the shake table and loaded. After initially loading the beam, no settlement occurred until an additional loading was applied.

connector is removed from the bottom of the setup. This then allows the system to be clamped to the table using the rail and some C-clamps. The system is also slightly adjusted by using small shims underneath the setup in order to level the test setup. To attach the mass to the setup, the hole at the top of the existing UTM connector is tapped. This then allows for a plate to be attached to a screw and screwed in to the center of the setup, with a large nut being used to hold the screw in place. From there, additional mass is added to the plate and clamped on using C-clamps.

The mass used for testing weighs 72.9 N, which is meant to represent the isolated payload. When this mass is applied to Beam 4, which had already been tested in Chapter 3, Beam 4 settles immediately. However, when this mass is applied to the virgin Beam 1, it is not enough to initially cause a displacement in the system, so it is manually forced through in order to cause it to settle into its operating range. The lack of settlement can be seen in Figure 4.1. Plastic deformation from excess loading is needed in order to get

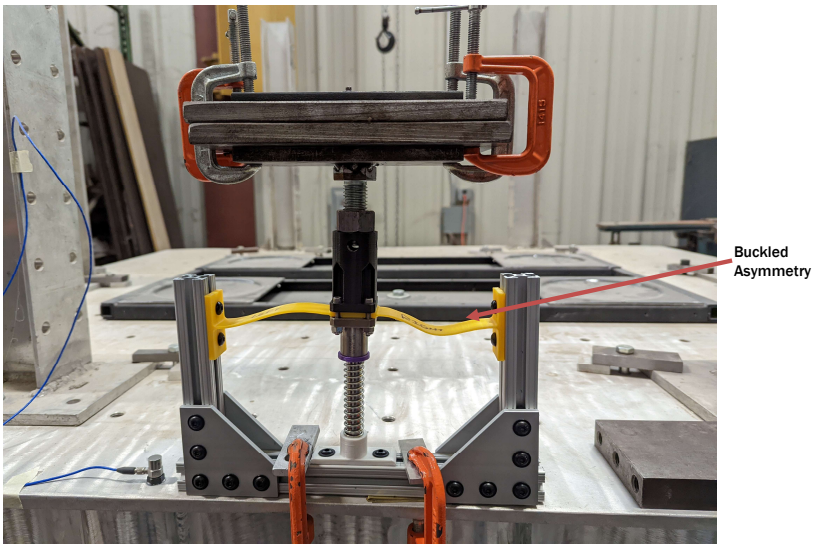

Figure 4.2: Following the addition of loading in order to create settlement, asymmetries were noted in the setup, where the right side buckled through and the left side did not.

the system to settle to its ideal operating range. After initially applying an additional loading to the beam, asymmetries could be noted in the plastic deformation, as can be seen in Figure 4.2. After additional loading is applied and additional plastic deformation is induced in the system, this asymmetry where only one side buckled could not be recreated.

For the testing, a time series of accelerations are generated using a MATLAB script, which adjusts to different parameters, including amplitude and frequency. These accelerations are converted into a time series of displacements and then transferred to a computer controlling the vertical shake table and a proprietary software for the computer. The computer reads the displacements and, using a series of six linear actuators, moves the shake table up and down in order to create the given displacements. The accelerations of the table and of the system are measured using high-sensitivity (100 mV/g), ceramic shear ICP accelerometers (352C33, PCB, Depew, NY) attached to both the table and to the mass. The accelerometer attached to the mass can be seen in Figure 4.3. The accelerations obtained from the accelerometers are measured using a separate

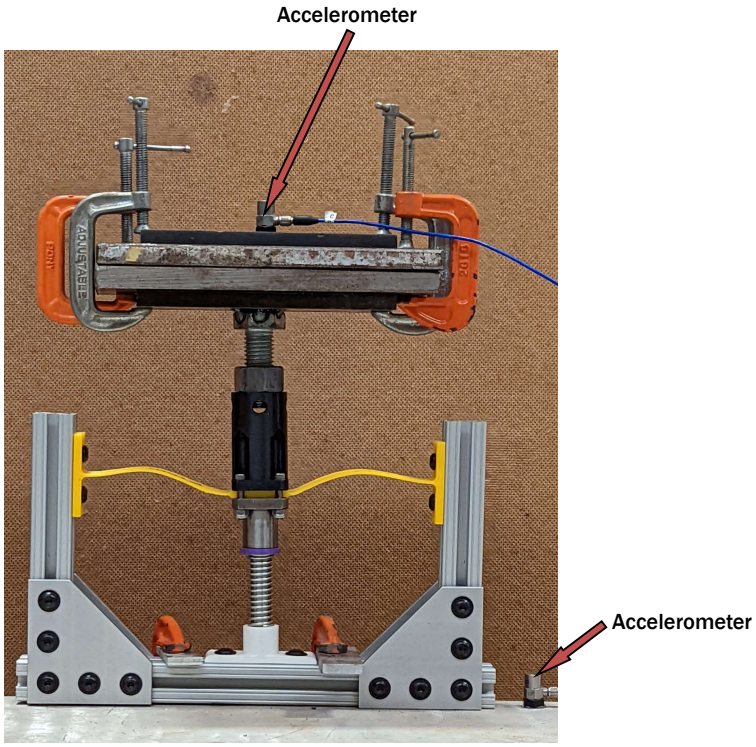

Figure 4.3: Accelerometers are attached to the mass and the shake table in order to measure accelerations.

computer using LabView and recorded for each test performed. The accelerometers measure accelerations at a rate of 5,000 Hz.

4.3 Dynamic Testing Sequence

Due to the importance of plastic deformation on the beam, the order the tests took place in is carefully recorded. This order is listed in Table 4.1.

4.4 Dynamic Testing Results For Harmonic Tests

The accelerations measured by the accelerometers are filtered in order to remove measurement noise. This is done by removing accelerations experienced at frequencies outside of an expected range. Frequencies outside of 0.5 Hz to 45 Hz are removed from the data. This aims to capture a significant range of frequencies that would be experi-

Table 4.1: Dynamic testing sequence on Beam 1 (virgin beam). Measurements are taken to determine plastic deformation before loading the system, following the initial loading, following the initial buckling of the setup, after Test No. 26, and after Test 31.

Test No.	Motion	Frequency [Hz]	Amplitude [$\%g$]
1	Harmonic	10	10
2		10	20
3		10	30
4		10	50
5		10	75
6		7.5	10
7		7.5	20
8		7.5	30
9		7.5	40
10		6.25	10
11		6.25	20
12		6.25	30
13		5	10
14		5	15
15		5	20
16		4	5
17		4	10
18		4	15
19		4	20
20		3.5	5
21		3.5	10
22		3	5
23		3	10
24		2.5	5
25		2.5	5
26		2.5	2.5
27		10	10
28		10	20
29		10	30
30		10	50
31		10	75
32	White noise	2–10	5*
33		5–20	5*
34		5–20	10*

*Root mean square (RMS) acceleration

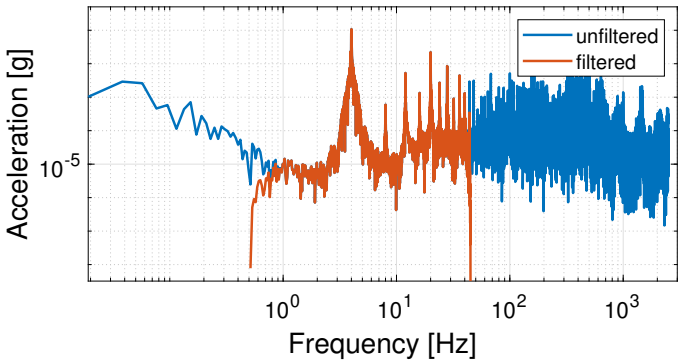

Figure 4.4: A fast Fourier transform showing the ground acceleration for the case of 4 Hz and 20%g. The data that is removed after filtering is shown in a different color than the data that is kept after filtering.

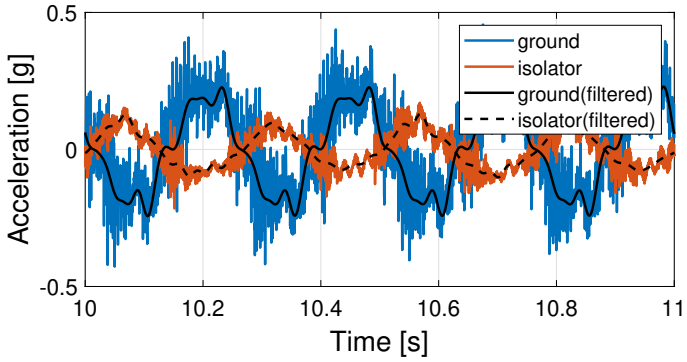

Figure 4.5: An acceleration time-history for the case of 4 Hz and 20 percent of a g showing the difference between the data before and after filtering.

enced by the system between tests, while removing environmental noise that would not have a significant impact on the accelerations experienced by the system. This allows for a significant amount of the noise to be removed from the system. An example of the noise removed from the system can be seen in Figures 4.4 and 4.5. Here, the frequencies removed in the filtering process can be seen in Figure 4.4. The removal of these frequencies causes the difference between the filtered data and the unfiltered data for Figure 4.5.

After the data is filtered, the data for each different test is processed and two different types of graphs are produced for each case.

The first type of graph used is an acceleration time-history graph. This shows how

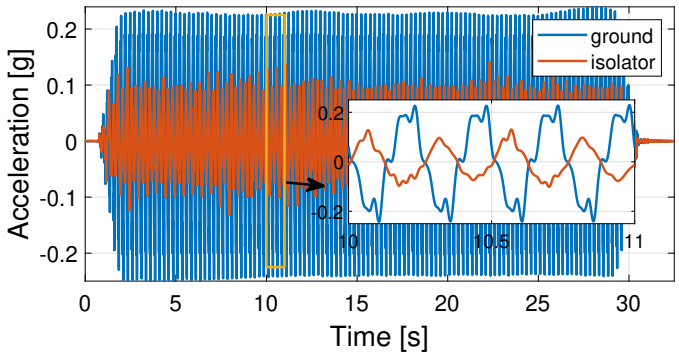

Figure 4.6: An acceleration time-history for the case of 4 Hz and 20%g showing the effects of the ground motion on the isolated mass.

the accelerations of the system changes over time, for both the ground and the isolation system. The time-history graph for the case of 4 Hz and 20%g is provided in Figure 4.6. For every case tested in this research (Table 4.1), the isolator moves out-of-phase with the ground motion. However, if the system were to be subjected to frequencies less than the natural frequency, it would be expected that it would move in-phase with the ground motion. Additional frequencies can be seen when examining the graph closely, but the forcing frequency is the dominant cause of acceleration experienced by the system. The time-history graph can be used to easily obtain the maximum accelerations experienced by both the ground and the isolator:

$$\text{peak ground acceleration} = a_g^{\max} = \max|\ddot{u}_g(t)| \tag{4.1}$$

$$\text{peak isolator acceleration} = a^{\max} = \max|\ddot{u}_g(t) + \ddot{u}(t)| \tag{4.2}$$

where $a_g^{\max}$ is the peak ground acceleration, $\ddot{u}_g(t)$ is the acceleration of the ground varying based off of time, $a^{\max}$ is the peak isolator acceleration, and $u(t)$ is the acceleration experienced by the isolator.

The second type of graph used is a fast Fourier transform (FFT). An FFT allows for accelerations to be attributed to different frequencies. The FFT for the case of 4 Hz and 20%g is provided in Figure 4.7. The majority of the accelerations are found directly at 4 Hz, but there is a noticeable spread between 3.5 Hz and 4.5 Hz. All cases tested

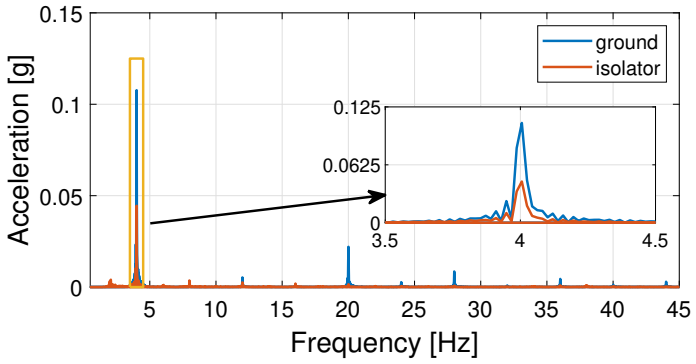

Figure 4.7: An FFT for the case of 4 Hz and 20%g showing the effects of the floor acceleration on the isolated mass.

have a spread in the accelerations about the expected point. Additionally, all cases have meaningful accelerations at integer multiples of the forcing frequency (e.g., 12 Hz and 8 Hz for the system excited at 4 Hz) and at half the forcing frequency (e.g., 2 Hz for the system excited at 4 Hz). This can be seen in the time-history graph as periodic accelerations within each wave of the forcing harmonic. These periodic accelerations can be found in both the ground motion and the isolator motion, indicating that these small motions are also passed through the structure, which also corroborates what was seen in the time-history. However, in the isolator these accelerations have a lower amplitude, as they are isolated out to a degree due to being at a higher frequency.

From these two different types of graphs, transmissibilities are able to be obtained for each different case for the sake of comparison. For determining transmissibility from the time-history graphs, the maximum absolute value of the filtered acceleration is taken for both the ground motion and the isolator motion and compared to one another:

$$\text{Transmissibility} = \frac{a^{\max}}{a_g^{\max}} \tag{4.3}$$

The filtered acceleration is used in order to remove effects from forces not intended to be considered in this experiment. For determining the transmissibility from the FFT graphs, the peak response acceleration for both the floor and isolator are taken from

the FFT in the vicinity of the forcing frequency and compared to one another. This peak response is always taken close to the forcing frequency; however, the discrete frequencies at which the FFT is calculated did not necessarily include the exact forcing frequency. Because of this, the transmissibility from the FFT is thought to be less accurate. Results from the transmissibility test can be found in Table 4.2 and Figures 4.8 and 4.9.

Table 4.2: Measured transmissibility values for each test performed during dynamic testing.

Forcing Frequency (Hz)	Acceleration (g)	Transmissibility from Time-History	Transmissibility from FFT	Notes
2.5	0.05	12.597	7.172	
2.5	0.05	16.225	7.766	
2.5	0.025	3.153	3.388	
3	0.05	1.528	1.274	
3	0.1	1.697	1.204	
3.5	0.05	1.055	0.850	
3.5	0.1	0.868	0.693	
4	0.05	0.681	0.658	
4	0.1	0.596	0.509	
4	0.15	0.537	0.431	
4	0.2	0.565	0.413	
5	0.1	0.691	0.368	
5	0.15	0.425	0.266	
5	0.2	0.374	0.252	
6.25	0.1	0.312	0.284	
6.25	0.2	0.283	0.162	
6.25	0.3	0.271	0.154	
7.5	0.1	0.302	0.232	
7.5	0.2	0.181	0.143	
7.5	0.3	0.157	0.104	
7.5	0.4	0.170	0.106	
10	0.1	0.249	0.240	Initial test results
10	0.2	0.221	0.131	
10	0.3	0.169	0.094	
10	0.5	0.094	0.066	
10	0.75	0.069	0.055	
10	0.1	0.137	0.116	Final test results
10	0.2	0.171	0.120	
10	0.3	0.157	0.101	
10	0.5	0.133	0.091	
10	0.75	0.114	0.074	

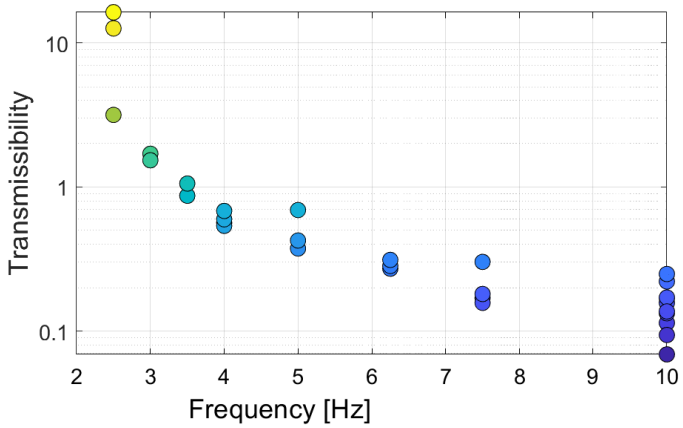

Figure 4.8: Transmissibility performance for system compared to forcing frequency. Transmissibility used is from peak response.

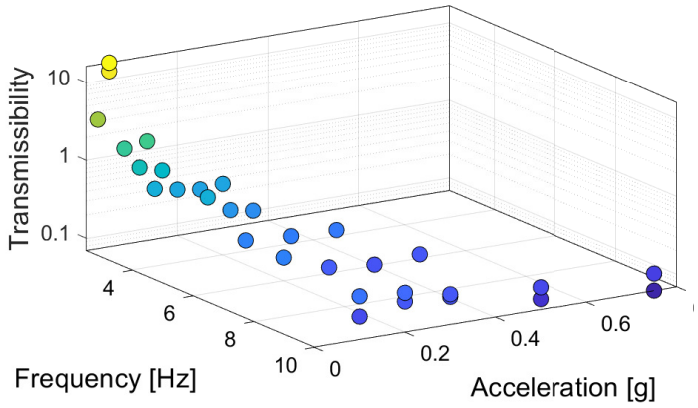

Figure 4.9: Transmissibility performance for system compared to forcing frequency and acceleration. Transmissibility used is from peak response.

The results produced several notable observations.

Firstly, the system consistently performs better under higher ground accelerations when compared to lower accelerations at the same frequencies. This indicates that the system is non-linear, as differing loads (or in the case of this research, accelerations) do not have a linear effect on the accelerations experienced by the structure. This could be due to the effects of or the nonlinear force-displacement response of the isolation system under large displacements. Although friction did not pose a large problem during static testing because the load head moved the bearing vertically up and down the shaft,

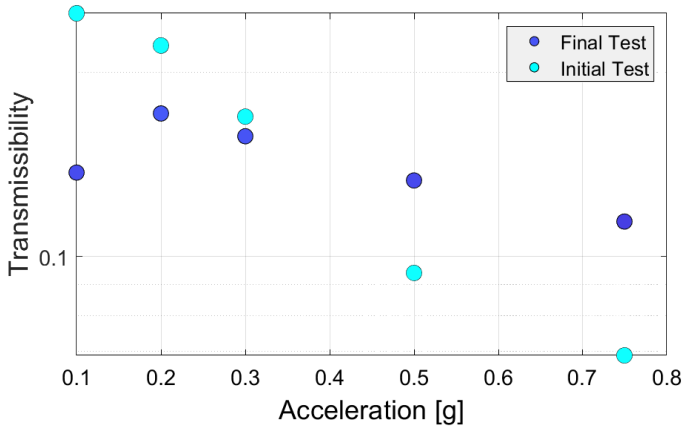

Figure 4.10: Transmissibility performance for system compared to ground acceleration. Transmissibility used is from peak response graph. All points are taken at a forcing frequency of 10 Hz.

moving in the shake table results in more free movement, thus causing movement in directions other than the vertical direction. This then causes the parts to rub up against each other, creating more friction. Friction force has a lesser effect when the structure is subjected to more violent ground accelerations because friction force is constant, but the input forcing ($m\ddot{u}_g$) increases with increasing $\ddot{u}_g$, thus causing the relative influence of friction to be less. From comparing the results for the tests performed at 10 Hz (Figure 4.10, which was done at the start and end of dynamic testing, this phenomenon is more prevalent in the initial set of tests when compared to the tests at the end of the experimentation. Because of this, the system has a more variable transmissibility depending on loading before plastic deformations have set in.

Secondly, at 2.5 Hz and 3 Hz, the system amplifies the effects of the accelerations at the base (i.e., transmissibility in excess of unity), resulting in higher accelerations experienced at the mass when compared to the accelerations experienced by the base. This indicates that the forcing frequency is close to reaching the natural frequency.

Thirdly, due to the motion of the structure, it is expected that it has at least one additional natural frequency, out of plane with the intended direction of motion of the system. Significant lateral motion is noted during the tests at 5 Hz, indicating that there

is a natural frequency close to 5 Hz. There is also slight lateral motion noted during the tests at 3.5 Hz and 2.5 Hz, but it did not seem significant in comparison to the vertical acceleration of the structure.

Fourthly, there is significant plastic deformation over the course of the experimentation on Beam 1. The height of the spring is measured several different times throughout the course of dynamic testing to measure the effects of plastic deformation. Initially, prior to loading, the spring's length was 76.0 mm. After the loading is initially applied, the spring's length dropped to 72.6 mm. After manually buckling the beam in order to get it to settle before testing, the spring's length drops to 54.4 mm. This shows that a significant deformation occurs upon reaching an initial loading for the first time. After going through every dynamic harmonic test, the spring's length was 47.6 mm. This indicates that the bulk of the plastic deformation occurs upon initial loading; however, there is still some slight creep as more loading occurs.

Dynamic testing results for white noise motion tests can be seen in Appendix D. Bulk dynamic testing results for all harmonic motion tests can be seen in Appendix E.

4.5 Summary

Dynamic testing is performed on the system using a vertical shake table. Both time-history analyses and FFTs are used to analyze the results. Results show that the system effectively produced isolation for forcing frequencies greater than 3.5 Hz. Unexpectedly, it is found that the system performed better under larger accelerations. Significant plastic deformation occurs in the design beam over the course of dynamic testing. This results in the system having different performances over time as plastic deformation occurs, even when subject to the same loading pattern.

Chapter 5
Summary, Conclusions, and Future Work

5.1 Summary and Conclusions

A light, small-scale vertical isolation system is designed and fabricated. It is designed under the intention that the scaling of the setup would be able to be adjusted such that valuable objects, such as a server cabinet, could be isolated following changes to the scaling of the system. This system is designed using the principles of negative stiffness for a pair of laterally loaded arches in combination with a parallel spring in order to obtain a desired force-displacement curve with a quasi-zero stiffness. Due to the usage of the 3D printer, this laterally loaded arch has its shape prescribed such that it is initially stress-free, despite having initial curvature.

In order to obtain force-displacement curves for the setup, three different methods are used: a mathematical energy minimization approach, an OpenSees finite element (FE) model, and characterization tests using an experimental setup. All three systems are modeled to represent the system designed in Chapter 3, meaning that every setup uses the same beam parameters and the same spring parameters. In order to accurately model the spring for all three methods, the spring is experimentally tested and is found to have a stiffness of 2.74 N/mm.

In Chapter 2, an energy minimization approach is used to model the behavior of the beam. Here, a mathematical model seeks to determine the optimal shape of the beam under a given displacement by attempting to find the most stable energy state of the

beam. Using this information, forces are able to be associated with the energy states and related to the displacement under a given force. From this method, the negative stiffness for the two beams is determined to be -2.17 N/mm and the positive stiffness of the combined setup is determined to be 0.57 N/mm.

Also in Chapter 2, an OpenSees FE model is used to analyze the behavior of the beam. Here, a FE model is created by discretizing the beam into 21 different nodes, corresponding to 20 different elastic, Euler-Bernoulli elements with corotational transformation. Afterwards, these elements are run through an earthquake simulation software (OpenSees) in order to determine the effects of increasing vertical load at a point of interest. From this method, the negative stiffness for the two beams was determined to be -2.09 N/mm and the positive stiffness of the combined setup is determined to be 0.65 N/mm.

In Chapter 3, an experimental setup was created. This experimental setup is tested using a universal testing machine, which controlled displacements and measured the amount of load needed to generate different displacements. This allows for repeated loads to be applied to the beams in order to determine how they worked in practice. Using this model, slight hysteresis is found in the system, differing from the energy minimization approach. Additionally, the effects of plastic deformation are able to be seen on the system, with the force-displacement curve changing with every cycle of loading and unloading. Using this experimental setup, three different beams are tested. From this setup, the average negative stiffness for the two beams is determined to be -2.09 N/mm and the average positive stiffness of the combined setup is determined to be 0.65 N/mm.

All three of the experimental setup stiffnesses are within the range of expected values determined from the theoretical models, as can be seen in Figure 3.14. This is especially the case when considering the large variation of beams due to the lack of

precision from the 3D printer used. Although the theoretical models do a good job of accurately predicting the general behavior of the system, the physical model contains significantly more information about the specific workings of the system. For example, the physical model showcases the vulnerability of the setup to asymmetries, which results in notable differences in the energy stored in the beam between sides of the beam. Additionally, the physical model could be better used to understand the effects of plastic deformation, friction, and variability between tests. Because of this, the physical model is believed to be the better model for interpreting the behavior of this particular setup. However, the theoretical models have the advantage of being more adaptable to different setups, as they can more quickly be adjusted since they do not require extreme precision.

In Chapter 4, the setup that the theoretical models are based off of and that static testing is performed on is subjected to vertical ground accelerations using a shake table. A design load is applied to the test setup in order to cause settling in the beam into the operating range. Harmonic ground accelerations are then applied to the setup, and the acceleration of the isolated mass was measured. The setup is found to exhibit isolation for forcing frequencies greater than 3.5 Hz. Isolation performance improves as both forcing frequency and acceleration increased. In fact, for the test at 10 Hz and $0.75g$, the transmissibility is found to be between 0.069 and 0.114, depending on the amount of plastic deformation in the beam. The natural frequency of the isolation system is determined to be between 2.5 Hz and 3 Hz.

From dynamic testing, several notable properties in the system are determined. Firstly, plastic deformation causes substantial effects in the system. From the results that are measured in dynamic testing, less variability is found in the setup after substantial testing has already occurred on the beam. Additionally, plastic deformation has a large effect on the shape of the beam, greatly increasing the amount of natural bowing

in the beam. Secondly, there is visible out-of-plane displacement that occurred in the setup, despite only vertical accelerations being applied to the system. It is believed that there is at least one other mode in the system, which has a natural frequency of 5 Hz. Thirdly, the impacts of acceleration on the transmissibility experienced by the isolated mass are unexpected. This indicates that the system is non-linear. Friction is expected to be what causes this non-linearity, as larger accelerations result in changes in the ratio of force applied at the base to the force due to friction being applied to the system.

Overall, the setup performs well for the expected ranges of frequencies intended to be isolated.

5.2 Future Work

This research seeks to design an isolation system that could be used for small-scale applications. As a continuation of this research, the following are several areas which have the potential for further investigation:

- Several different test setups could be used in parallel in order to isolate a larger mass. This would have several advantages compare to the system used in this research. Firstly, it would allow for a larger load to be isolated, more closely mimicking the loading of a server cabinet or a piece of biomedical equipment which may be sensitive and require isolation in order to protect. Secondly, it would allow for the effects of lateral motion to be explored. Ultimately, combining several different isolation systems together in order to isolate in multiple different directions would prove useful for protecting certain objects.

- The initial shape of the beam could be explored more in-depth in order to provide different force-displacement curves. As was mentioned in Chapter 2, changing the initial seeding of different mode shapes ($q_n = Q_{n,0}/H$) into the beams resulted in different force-displacement curve shapes. From testing using the energy min-

imization approach, adjusting q_1 and q_3 could result in creating a quasi-zero stiffness without a spring. However, this results in losing out on a substantial amount of the initial positive stiffness of the beam due to q_1. Further research could be done into this in order to determine whether there is an effective method of creating an initial positive stiffness using another method, and perhaps a system could be designed without a spring.

- Different beam parameters could be used in order to create different effects in the force-displacement curves of the system, and with it the dynamic properties of the setup. For example, the material of the beam could be substituted from plastic to carbon fiber, effectively changing the Young's modulus of the beam and with it the energy stored in the beam. This has the disadvantage of requiring a different method of fabricating a beam, however. Additionally, springs at the correct stiffness could be hard to find if the beam is too much stiffer. Furthermore, beams could be adjusted such that they have different rises, lengths, and cross sections, in order to meet the needs of a system. The theoretical models used allow for these changes to be quickly explored in order to determine the efficacy of changes before being produced.

Bibliography

ASCE (2017). *Minimum Design Loads and Associated Criteria for Buildings and Other Structures*. American Society of Civil Engineers (ASCE), ASCE/SEI 7-16 edition.

Baumgart (2000). "Stiffness — an unknown world of mechanical science?." *Injury*, 31, 14–84. doi:https://doi.org/10.1016/S0020-1383(00)80040-6.

Buckle, I. G. and Mayes, R. L. (1990). "Seismic isolation: History, application, and performance–a world view." *Earthquake Spectra*, 6(2), 161–201. doi: 10.1193/1.1585564.

Cain, T. M. N. (2020). "Designing and characterizing negative stiffness devices for apparent weakening and vertical isolation." M.S. thesis, University of Oklahoma, Norman, OK (May).

Cui, S., Bruneau, M., and Constantinou, M. C. (2012). "Integrated design methodology for isolated floor systems in single-degree-of-freedom structural fuse systems." *Report No. MCEER-12-0004*, MCEER.

Deng, T., Wen, G., Ding, H., Lu, Z.-Q., and Chen, L.-Q. (2020). "A bio-inspired isolator based on characteristics of quasi-zero stiffness and bird multi-layer neck." *Mechanical Systems and Signal Processing*, 145, 106967. doi:10.1016/j.ymssp.2020.106967.

Fulcher, B., Shahan, D., Haberman, M., Seepersad, C., and Wilson, P. (2014a). "Analytical and experimental investigation of buckled beams as negative stiffness elements for passive vibration and shock isolation systems." *Journal of Vibration and Acoustics*, 136, 031009. doi:10.1115/1.4026888.

Fulcher, B. A., Shahan, D. W., Haberman, M. R., Conner Seepersad, C., and Wilson, P. S. (2014b). "Analytical and experimental investigation of buckled beams as negative stiffness elements for passive vibration and shock isolation systems." *Journal of Vibration and Acoustics*, 136(3), 031009. doi:10.1115/1.4026888.

Harrison, H. B. (1978). "Post-buckling behaviour of elastic circular arches." *ICE Proceedings*, 65, 283–298. doi:10.1680/iicep.1978.2946.

Harvey, Philip S., J., Wiebe, R., and Cain, T. M. N. (2020). "Inextensibility and Its Effect on the Number of Equilibria of Shallow Buckled Beams." *Journal of Applied Mechanics*, 87(12) 121007, doi:10.1115/1.4048199.

Harvey, Jr., P. S. and Kelly, K. C. (2016). "A review of rolling-type seismic isolation: Historical development and future directions." *Engineering Structures*, 125, 521–531. doi:10.1016/j.engstruct.2016.07.031.

Harvey, Jr., P. S. and Virgin, L. N. (2015). "Coexisting equilibria and stability of a shallow arch: Unilateral displacement-control experiments and theory." *International Journal of Solids and Structures*, 54, 1–11. doi:10.1016/j.ijsolstr.2014.11.016.

Harvey, Jr., P. S., Virgin, L. N., and Tehrani, M. H. (2019). "Buckling of elastic columns with second-mode imperfections." *Meccanica*, 1245(8), 1245–1255. doi: 10.1007/s11012-019-01025-z.

Iwan, W. D. (1978). "The earthquake design and analysis of equipment isolation systems." *Earthquake Engineering and Structural Dynamics*, 6(12), 523–534. doi: 10.1002/eqe.4290060602.

Kalantari, A. and Moayyedi, S. A. (2018). "Seismic vertical component effects on seismic demands of a base isolated bridge with friction- rubber bearings." *Civil Engineering Research Journal*, 3. doi:10.19080/CERJ.2018.03.555617.

Klasson, A., Crocetti, R., and Hansson, E. F. (2016). "Slender steel columns: How they are affected by imperfections and bracing stiffness." *Structures*, 8, 35–43. doi: 10.1016/j.istruc.2016.08.004.

Lago, A., Faridani, H. M., and Trabucco, D. (2018). "Structural engineering: Damping technologies for tall buildings." *CTBUH Journal*, (3), 42–47.

Lan, C.-C., Yang, S.-A., and Wu, Y.-S. (2014). "Design and experiment of a compact quasi-zero-stiffness isolator capable of a wide range of loads." *Journal of Sound and Vibration*, 333(20), 4843–4858. doi:10.1016/j.jsv.2014.05.009.

Leavitt, J., Jabbari, F., and Bobrow, J. E. (2007). "Optimal performance of variable stiffness devices for structural control." *Journal of Dynamic Systems, Measurement, and Control*, 129, 171–177. doi:10.1115/1.2432360.

Lee, C.-M., Goverdovskiy, V. N., and Temnikov, A. I. (2007). "Design of springs with "negative" stiffness to improve vehicle driver vibration isolation." *Journal of Sound and Vibration*, 302(4), 865–874. doi:10.1016/j.jsv.2006.12.024.

Liu, X., Xiuchang, H., and Hua, H. (2013). "On the characteristics of a quasi-zero stiffness isolator using euler buckled beam as negative stiffness corrector." *Journal of Sound and Vibration*, 332, 3359–3376. doi:10.1016/j.jsv.2012.10.037.

McKenna, F. and Feneves, G. L. (2000). *Open System for Earthquake Engineering Simulation (OpenSees)*. Pacific Earthquake Engineering Research Center, University of California, Berkeley, CA, version 2.5.0 edition.

Najafijozani, M., Becker, T. C., and Konstantinidis, D. (2020). "Evaluating adaptive vertical seismic isolation for equipment in nuclear power plants." *Nuclear Engineering and Design*, 358, 110399. doi:10.1016/j.nucengdes.2019.110399.

Pi, Y.-L., Bradford, M., and Tin-Loi, F. (2007). "Nonlinear analysis and buckling of elastically supported circular shallow arches." *International Journal of Solids and Structures*, 44, 2401–2425. doi:10.1016/j.ijsolstr.2006.07.011.

Plaut, R. H. (2015). "Snap-through of shallow extensible arches under unilateral displacement control." *Journal of Applied Mechanics*, 82(9), 094503. doi:10.1115/1.4030741.

Polymaker (2017). *PolyLite^{TM} PLA Technical Data Sheet*. Polymaker (June).

Porter, J. H., Cain, T. M., Fox, S. L., and Harvey, Jr., P. S. (2019). "Influence of infill properties on flexural rigidity of 3D-printed structural members." *Virtual and Physical Prototyping*, 14(2), 148–159. doi:10.1080/17452759.2018.1537064.

Schaer, F. (1909). "Foundation for building" (March). US Patent App. US951028A.

Shaw, A. D., Neild, S. A., and Wagg, D. J. (2013). "Dynamic analysis of high static low dynamic stiffness vibration isolation mounts." *Journal of Sound and Vibration*, 332(6), 1437–1455. doi:10.1016/j.jsv.2012.10.036.

Szolomicki, J. and Golasz-Szolomicka, H. (2019). "Technological advances and trends in modern high-rise buildings." *Buildings*, 9(9). doi:10.3390/buildings9090193.

Tehrani, M. H. and Harvey, Jr., P. S. (2019). "Generation of synthetic accelerograms for telecommunications equipment: fragility assessment of a rolling isolation system." *Bulletin of Earthquake Engineering*, 17, 1715–1737. doi:10.1007/s10518-018-0505-7.

Thompson, J. M. T. and Hunt, G. W. (1983). "On the buckling and imperfection-sensitivity of arches with and without prestress." *International Journal of Solids and Structures*, 19(5), 445–459. doi:10.1016/0020-7683(83)90055-0.

Wang, S., Xin, W., Ning, Y., Li, B., and Hu, Y. (2020). "Design, experiment, and improvement of a quasi-zero-stiffness vibration isolation system." *Applied Sciences*, 10(7). doi:10.3390/app10072273.

Yan, S.-T., Shen, X., Chen, Z., and Jin, Z. (2018). "Collapse behavior of non-uniform shallow arch under a concentrated load for fixed and pinned boundary conditions." *International Journal of Mechanical Sciences*, 137, 46–67. doi:10.1016/j.ijmecsci.2018.01.005.

Yang, J., Sato, T., Savidis, S., and Li, X. (2002). "Horizontal and vertical components of earthquake ground motions at liquefiable sites." *Soil Dynamics and Earthquake Engineering*, 22(3), 229–240. doi:10.1016/S0267-7261(02)00010-6.

Zhou, Y., Chen, P., and Mosqueda, G. (2019). "Analytical and numerical investigation of quasi-zero stiffness vertical isolation system." *Journal of Engineering Mechanics*, 145(6), 04019035. doi:10.1061/(ASCE)EM.1943-7889.0001611.

Appendix A
Preliminary Designs

The initial design tested in this research considers a flat, 203.2 mm long 3D-printed beam. This beam is supported by pinned connections (modeled with V-shaped grooves) and attempts to simulate a point load for the load. An example of this beam and the connections can be seen in Figure A.1. Several optimizations to this test setup are eventually made in order to improve the performance of the system. The beams used here have issues with snapping-through to different deflected shapes as load increased and decreased due to instabilities in the force-displacement curve.

The beams are tested in an Instron machine, which allows for displacement control,

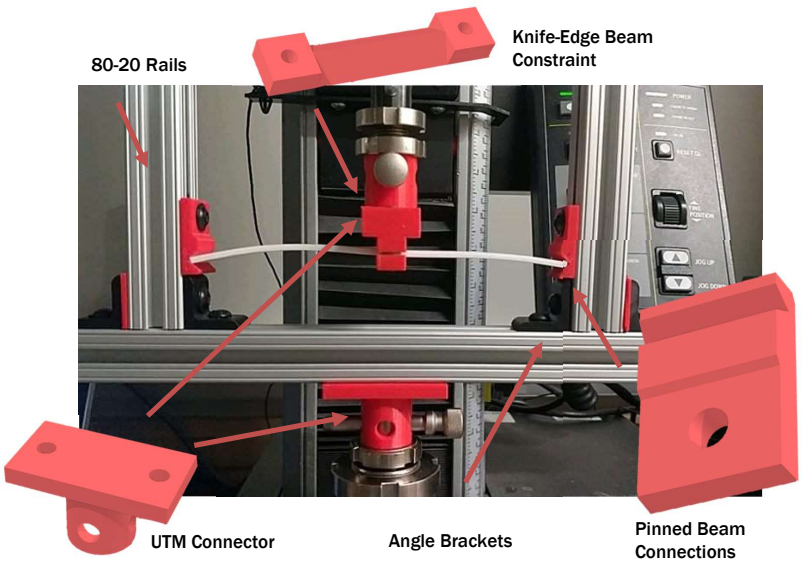

Figure A.1: Initial test setup

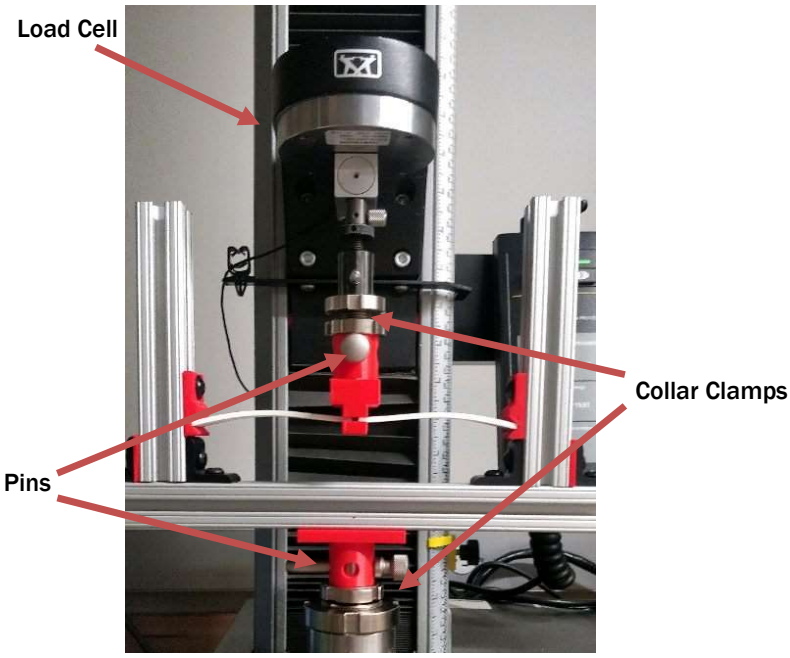

Figure A.2: Initial test setup placed in Instron machine.

with a given displacement requiring a certain force, which is measured using a load cell. The test setup is attached to the system using 3D-printed UTM (universal testing machine) connectors which are pinned to the Instron machine and clamped, as can be seen in Figures A.1 and A.2.

Eventually, springs are added to the test setup in order to attempt to achieve quasi-zero stiffness. A redesigned load-head is designed and 3D-printed in order to accommodate the addition of the springs to the design. The redesign can be seen in Figure A.3.

In addition to the springs, this adjusted setup also adds a flat platform with which load could be applied to the setup in order to begin performing dynamic testing. Furthermore, it also adds guides in order to help improve the stability of the system as it is loaded.

After static tests on the setup with springs are finished, dynamic testing was ready

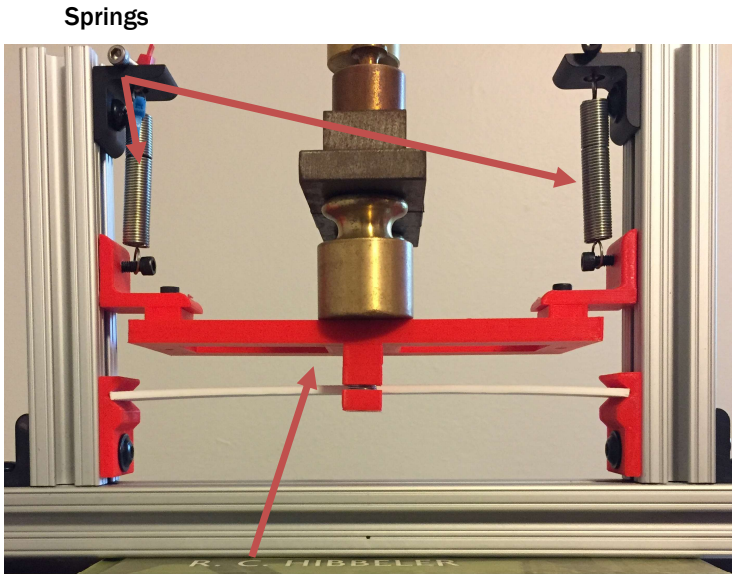

Figure A.3: Initial test setup with springs

to be performed. However, due to COVID-19, the vertical shake table was unable to be used. As a substitute for the dynamic testing, the setup is loaded with different masses and photographs were taken. An example photograph can be seen in Figure A.3. From the photographs, locations at various points on the beam are used in order to map out the deflected shape using a series of Fourier transforms Harvey et al. (2019). Additionally, the data is normalized for both length, as the length varied slightly from test to test due to slight movements in the camera, as well as for the deflection. This then allows for the deflections to be compared to one another and a relationship between mass and deflection to be determined. During this testing, a snapthrough occurred twice. This causes a large jump on the load deflection curve. The results of these tests can be seen in Figure A.4. Dynamic testing is never performed on this setup, but it is anticipated that this system would not have performed well in a dynamic test due to the stability issues.

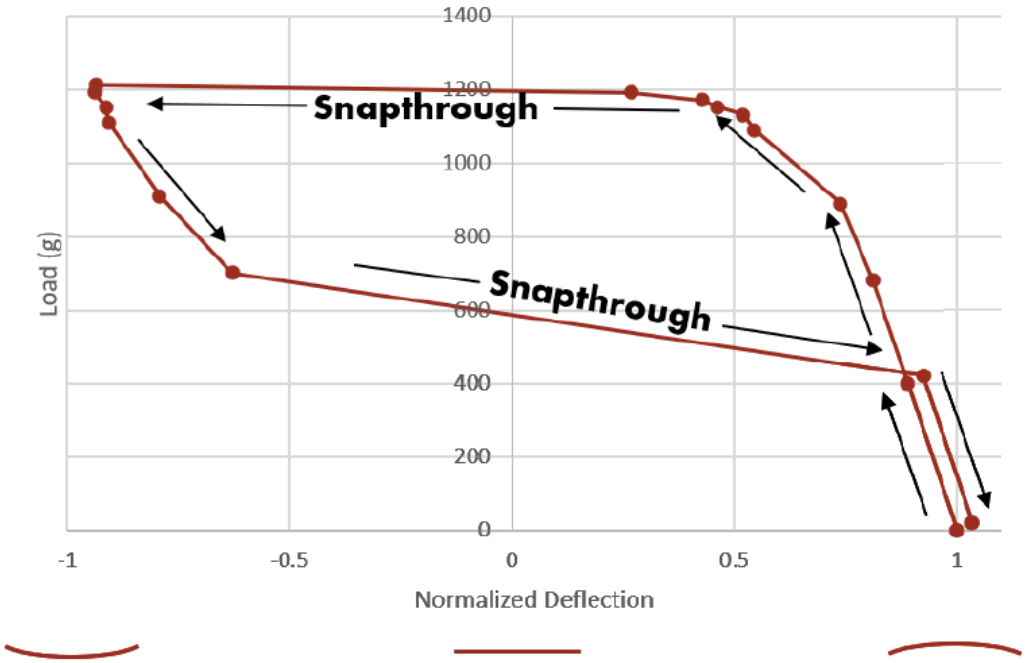

Figure A.4: Force-displacement results with old system. Beam snaps through during both loading and unloading.

Appendix B
Theoretical Results

B.1 Energy Minimization Model

Figures B.1 through B.3 include force-displacement curves for the beams and the combined setups for varying levels of initial third mode shape function seeding, q_3.

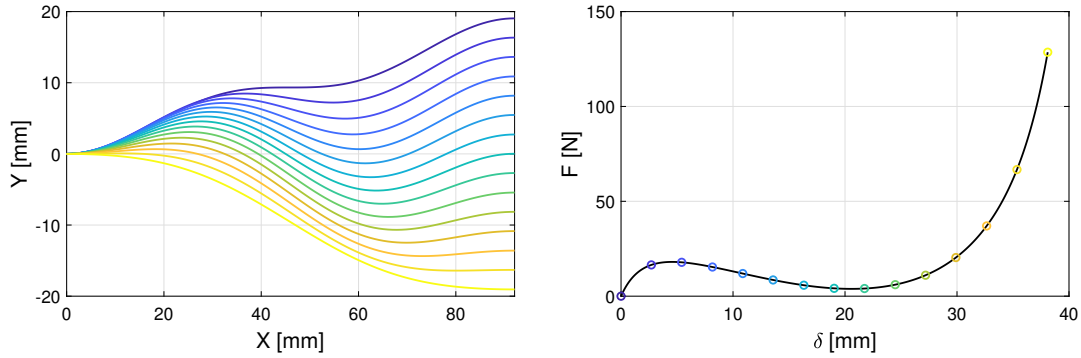

Figure B.1: Theoretical displacement history (left) and force-displacement curve (right) for the design beam and spring using the energy minimization model and $q_1 = 0.75$, $q_2 = -0.01$, and $q_3 = 0.25$.

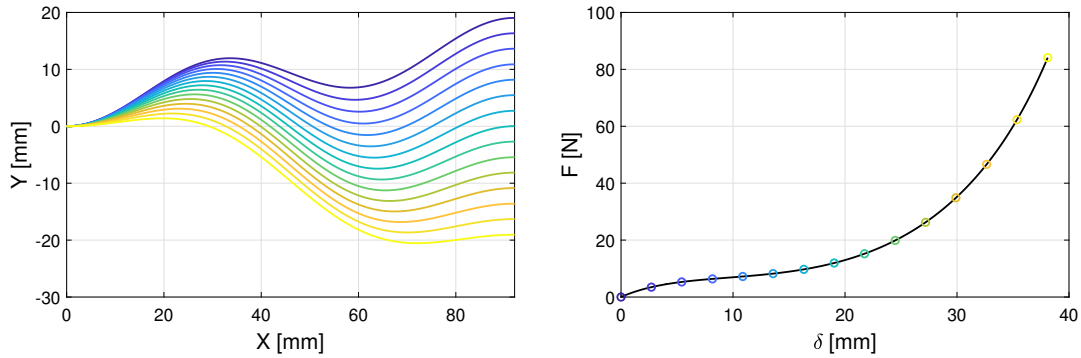

Figure B.2: Theoretical displacement history (left) and force-displacement curve (right) for the design beam and spring using the energy minimization model and $q_1 = 0.50$, $q_2 = -0.01$, and $q_3 = 0.50$.

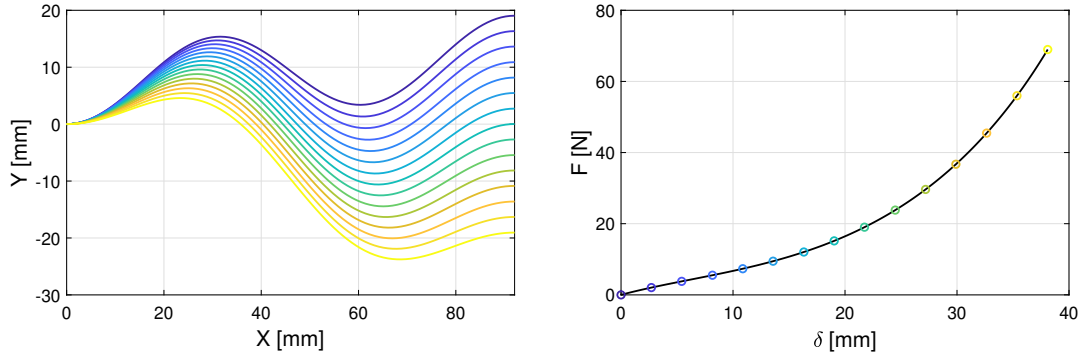

Figure B.3: Theoretical displacement history (left) and force-displacement curve (right) for the design beam and spring using the energy minimization model and $q_1 = 0.25$, $q_2 = -0.01$, and $q_3 = 0.75$.

Appendix C
OpenSees Model

Below is the OpenSees code `snapThroughAnalysis.tcl` used to model the laterally-loaded arch with a spring in parallel.

```
#=================================================================
#                SET UP
#=================================================================
wipe;                                  # clear memory of all past model
    definitions
model BasicBuilder -ndm 2 -ndf 3;    # Define the model builder, ndm=#
    dimension, ndf=#dofs
set folder Data;                       # set up name of data directory
file mkdir $folder;                    # create data directory

#=================================================================
#            DEFINED NODES
#=================================================================
node  1 0 0
node  2 4.604 0.117268551
node  3 9.208 0.466186664
node  4 13.812  1.038162818
node  5 18.416  1.819113063
node  6 23.02 2.789807814
node  7 27.624  3.926345347
node  8 32.228  5.200740339
node  9 36.832  6.581612956
node  10  41.436  8.034961535
node  11  46.04 9.52499981
node  12  50.644  11.01503809
node  13  55.248  12.4683867
node  14  59.852  13.84925936
node  15  64.456  15.1236544
node  16  69.06 16.260192
node  17  73.664  17.23088681
node  18  78.268  18.0118371
node  19  82.872  18.5838133
node  20  87.476  18.93273144
```

```
node  21  92.08 19.05

node    22  92.08 19.05

#=================================================================
#           BOUNDARY CONDITIONS
#=================================================================
fix 1 1 1 1
fix 21 1 0 1
fix 22 1 1 1

#=================================================================
#           DEFINE MATERIALS & SECTIONS
#=================================================================
set nbeam 2
set Es [expr $nbeam*2636]
set A 40.323
set Iz 8.468

#=================================================================
#           DEFINE ELEMENTS
#=================================================================

geomTransf Corotational  1;        # Corotational

element elasticBeamColumn   1 1   2   $A  $Es $Iz 1
element elasticBeamColumn   2 2   3   $A  $Es $Iz 1
element elasticBeamColumn   3 3   4   $A  $Es $Iz 1
element elasticBeamColumn   4 4   5   $A  $Es $Iz 1
element elasticBeamColumn   5 5   6   $A  $Es $Iz 1
element elasticBeamColumn   6 6   7   $A  $Es $Iz 1
element elasticBeamColumn   7 7   8   $A  $Es $Iz 1
element elasticBeamColumn   8 8   9   $A  $Es $Iz 1
element elasticBeamColumn   9 9   10  $A  $Es $Iz 1
element elasticBeamColumn   10 10  11  $A  $Es $Iz 1
element elasticBeamColumn   11 11  12  $A  $Es $Iz 1
element elasticBeamColumn   12 12  13  $A  $Es $Iz 1
element elasticBeamColumn   13 13  14  $A  $Es $Iz 1
element elasticBeamColumn   14 14  15  $A  $Es $Iz 1
element elasticBeamColumn   15 15  16  $A  $Es $Iz 1
element elasticBeamColumn   16 16  17  $A  $Es $Iz 1
element elasticBeamColumn   17 17  18  $A  $Es $Iz 1
element elasticBeamColumn   18 18  19  $A  $Es $Iz 1
element elasticBeamColumn   19 19  20  $A  $Es $Iz 1
element elasticBeamColumn   20 20  21  $A  $Es $Iz 1

uniaxialMaterial Elastic 1 2.74
element zeroLength 21 21 22 -mat 1 -dir 2

#=================================================================
#           Define RECORDERS
#=================================================================
```

```
recorder Node -file $folder/nodeDispl.out -node 1 2 3 4 5 6 7 8 9 10 11 12 13 14 15 16 17 18 19 20 21 22  -dof 1 2 3 disp;
recorder Node -file $folder/endReactions.out -node 1 22 -dof 1 2 3 reaction;

#=================================================================
#                    DEFINE VERTICAL LOADS
#=================================================================
pattern Plain 100 "Linear" {
    load    21  0.0 -1.0 0.0;
}

#=================================================================
#                    SAVE NODAL INFORMATION
#=================================================================
set nodeXYZ "${folder}/Nodes.txt"
set NODES [open $nodeXYZ "w"]
foreach i [list 1 2 3 4 5 6 7 8 9 10 11 12 13 14 15 16 17 18 19 20 21 22] {
    puts $NODES "$i [nodeCoord $i]"
}
close $NODES

#=================================================================
#               START OF ANALYSIS
#=================================================================
# Create the convergence test
test EnergyIncr  1.0e-18 100
#test NormDispIncr 1.0e-8    50     0
#test NormUnbalance 1.0e-6 400 1

algorithm  Newton
numberer RCM
constraints Plain

set maxD 38.2
set numIncr 20000
set dD [expr -$maxD/$numIncr]
integrator DisplacementControl 21 2 $dD

analysis Static
# system FullGeneral

#=================================================================
#             PERFORM ANALYSIS
#=================================================================
analyze $numIncr

loadConst -time 0.0

puts "################################################"
puts "Analysis Complete"
```

```
133 puts "################################################"
134
135 wipe
```

Appendix D
Dynamic Testing White Noise Results

The isolation system discussed in Chapters 3 and 4 was subjected to three different white noise tests. The dynamic tests follow the procedure mentioned in Chapter 4. These tests sought to broaden the spectra of the transmissibility curve for the isolation system. Each of these tests lasted 60 seconds. These tests would have produced cleaner fast Fourier transforms had a longer test duration been used, as more relationships between acceleration and frequency would have been developed. Despite this, trends can still be seen in the FFTs for the different white noise tests performed.

Figures D.1 and D.2 include acceleration time-histories and FFTs, respectively, for white noise generated with frequencies between 2 Hz and 10 Hz and with accelerations that have a root mean square (RMS) of 0.05g.

Figures D.3 and D.4 include acceleration time-histories and FFTs, respectively, for white noise generated with frequencies between 5 Hz and 20 Hz and with accelerations that have an RMS of 0.05g.

Figures D.5 and D.6 include acceleration time-histories and FFTs, respectively, for white noise generated with frequencies between 5 Hz and 20 Hz and with accelerations that have an RMS of 0.10g.

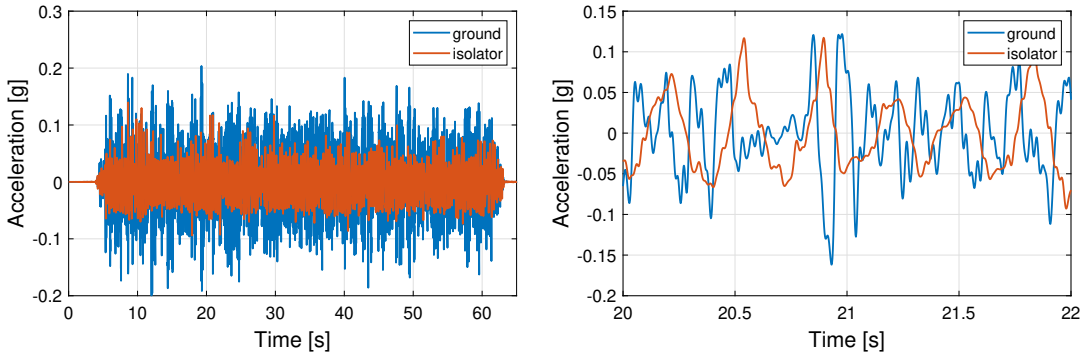

Figure D.1: Time history for full duration of white noise test (left) and zoomed in on two second interval (right) for frequencies from 2-10 Hz and accelerations that have an RMS of 0.05g.

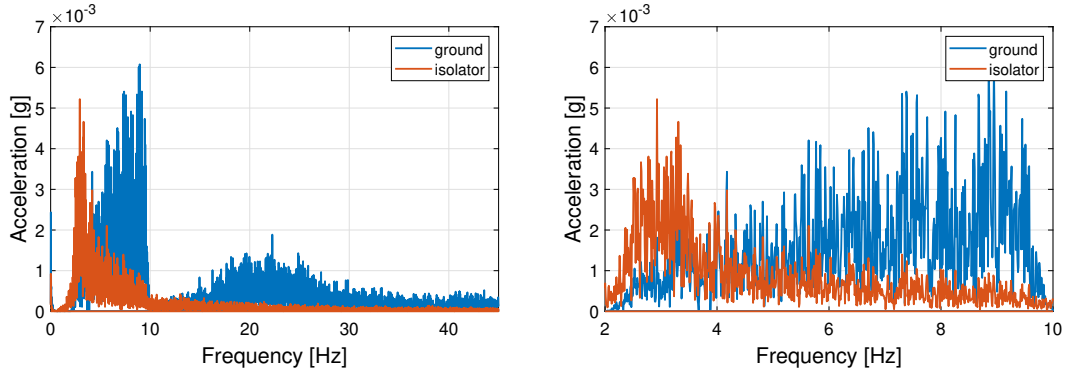

Figure D.2: FFT for full range of filtered frequencies (left) and zoomed in on frequencies that the shake table was displaced at (right) for frequencies from 2-10 Hz and accelerations that have an RMS of 0.05g.

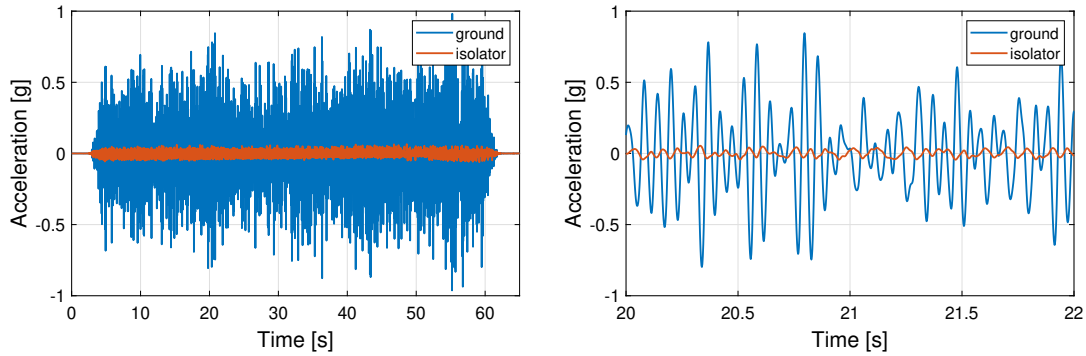

Figure D.3: Time history for full duration of white noise test (left) and zoomed in on two second interval (right) for frequencies from 5-20 Hz and accelerations that have an RMS of 0.05g.

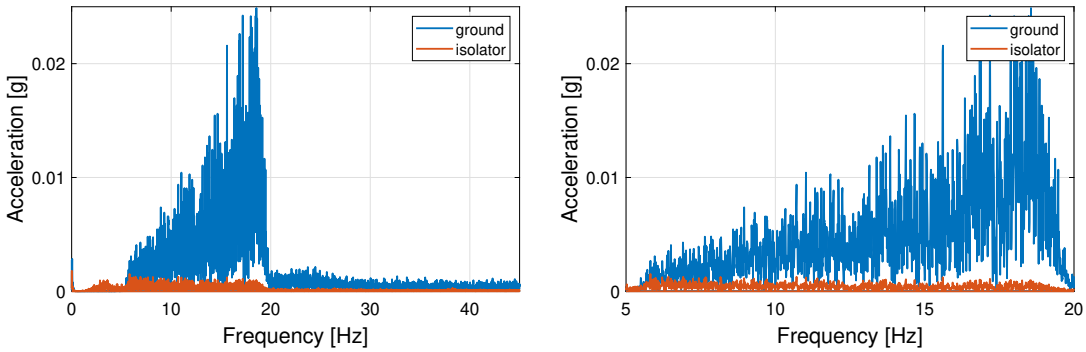

Figure D.4: FFT for full range of filtered frequencies (left) and zoomed in on frequencies that the shake table was displaced at (right) for frequencies from 5-20 Hz and accelerations that have an RMS of 0.05g.

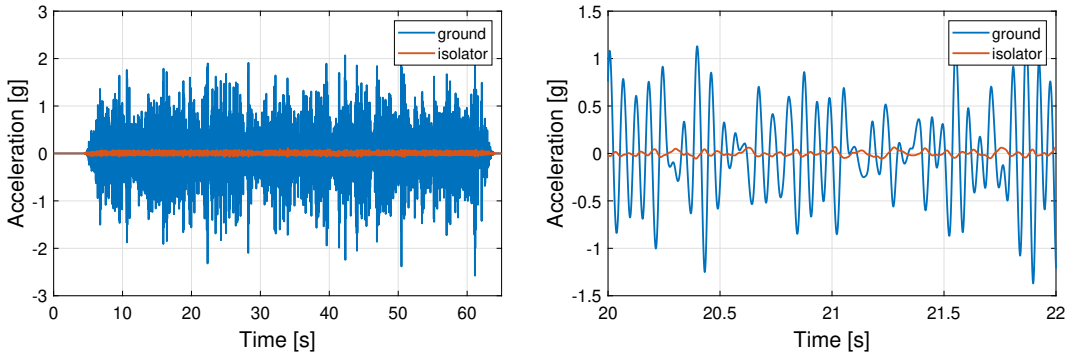

Figure D.5: Time history for full duration of white noise test (left) and zoomed in on two second interval (right) for frequencies from 5-20 Hz and accelerations that have an RMS of 0.10g.

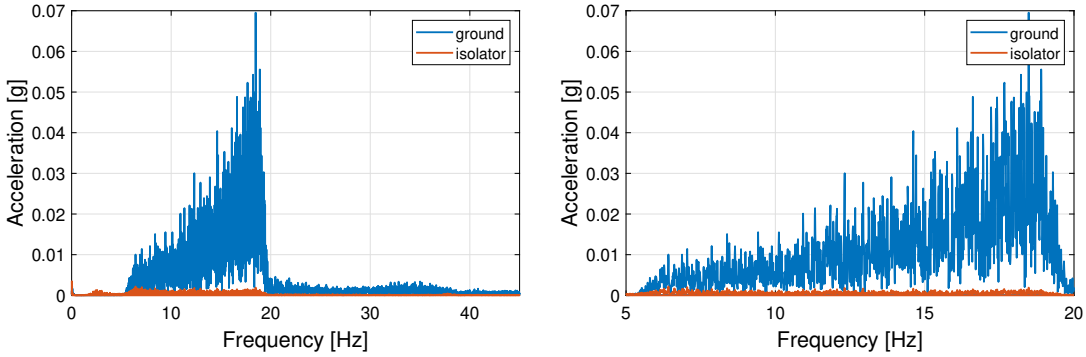

Figure D.6: FFT for full range of filtered frequencies (left) and zoomed in on frequencies that the shake table was displaced at (right) for frequencies from 5-20 Hz and accelerations that have an RMS of 0.10g.

Appendix E
Dynamic Testing Harmonic Bulk Results

This Appendix contains bulk results for all of the different harmonic dynamic tests performed on the system. Figures are listed in the order that the tests were performed in (Table 4.1). Figures include acceleration time-histories and fast Fourier transforms (FFT).

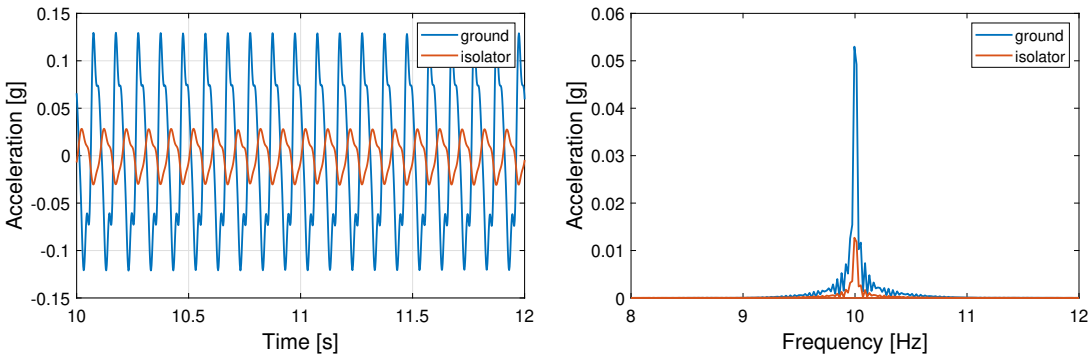

Figure E.1: Acceleration time-history for two-second interval of harmonic test (left) and FFT ± 2 Hz of the forcing frequency (right). Test 1 at a frequency of 10 Hz and amplitude of $0.1g$.

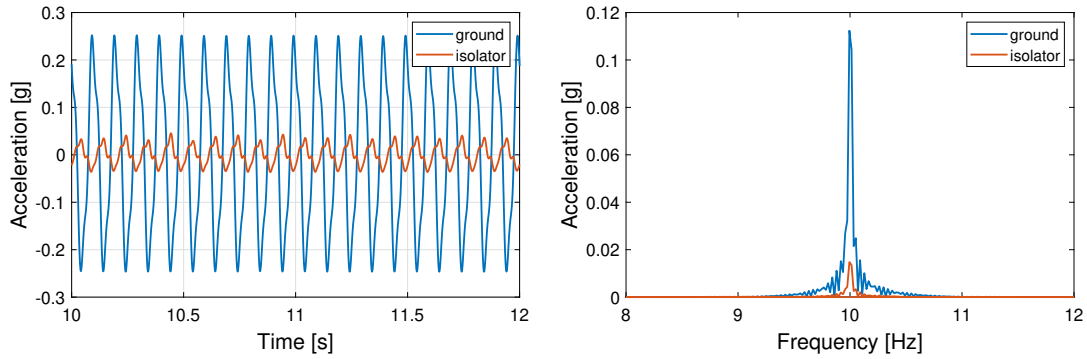

Figure E.2: Acceleration time-history for two-second interval of harmonic test (left) and FFT ± 2 Hz of the forcing frequency (right). Test 2 at a frequency of 10 Hz and amplitude of $0.2g$.

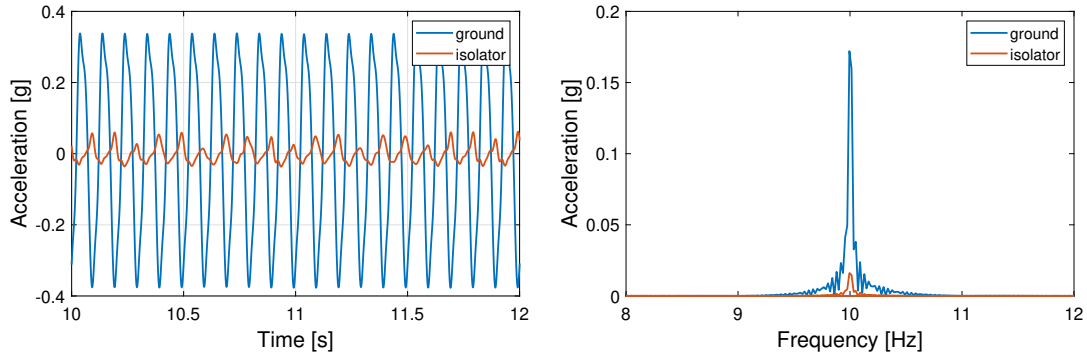

Figure E.3: Acceleration time-history for two-second interval of harmonic test (left) and FFT ± 2 Hz of the forcing frequency (right). Test 3 at a frequency of 10 Hz and amplitude of $0.3g$.

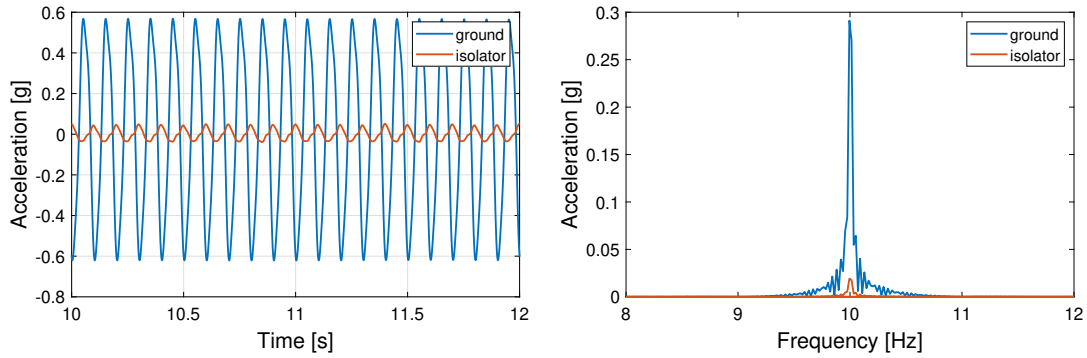

Figure E.4: Acceleration time-history for two-second interval of harmonic test (left) and FFT ± 2 Hz of the forcing frequency (right). Test 4 at a frequency of 10 Hz and amplitude of $0.5g$.

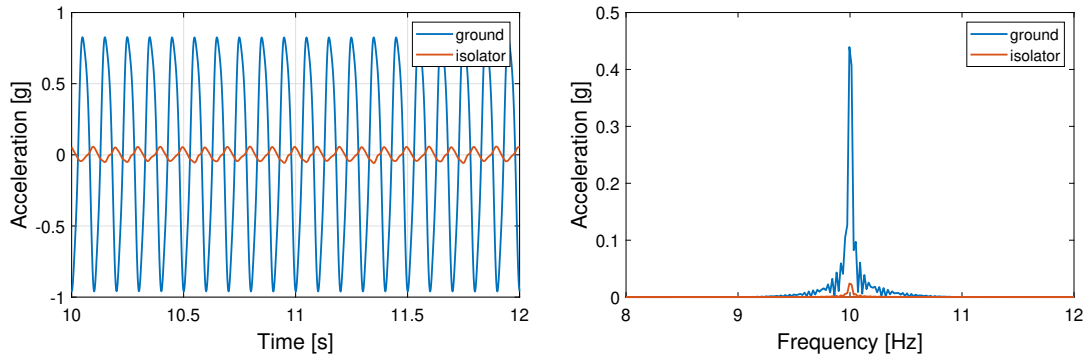

Figure E.5: Acceleration time-history for two-second interval of harmonic test (left) and FFT ±2 Hz of the forcing frequency (right). Test 5 at a frequency of 10 Hz and amplitude of 0.75g.

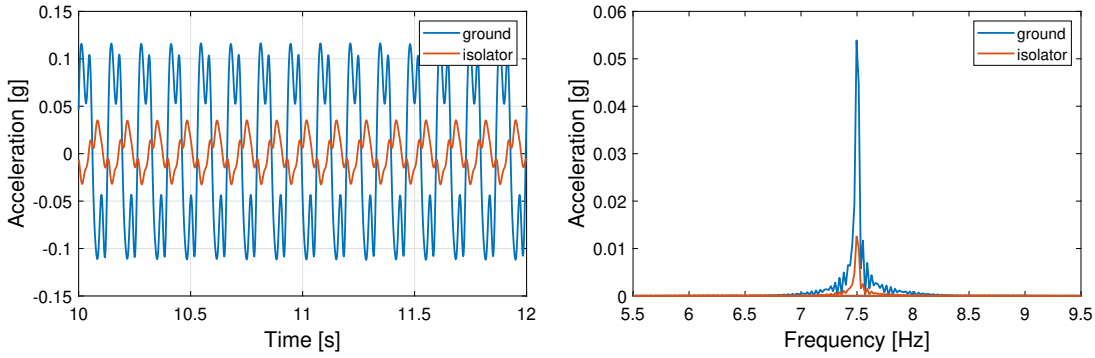

Figure E.6: Acceleration time-history for two-second interval of harmonic test (left) and FFT ±2 Hz of the forcing frequency (right). Test 6 at a frequency of 7.5 Hz and amplitude of 0.10g.

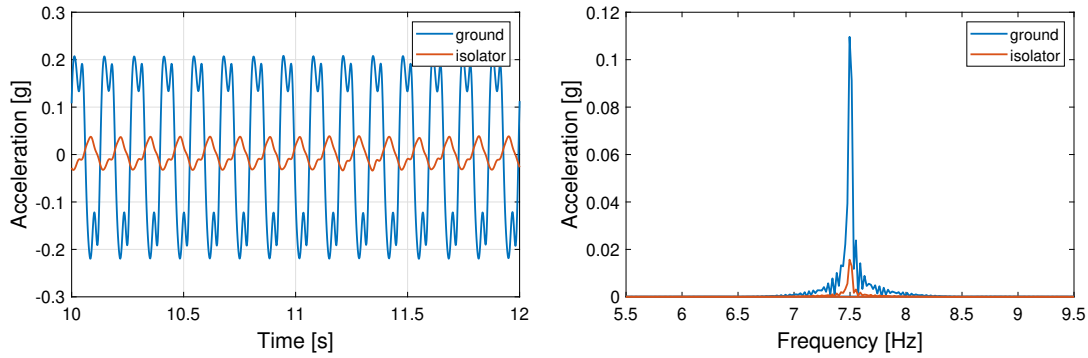

Figure E.7: Acceleration time-history for two-second interval of harmonic test (left) and FFT ±2 Hz of the forcing frequency (right). Test 7 at a frequency of 7.5 Hz and amplitude of 0.20g.

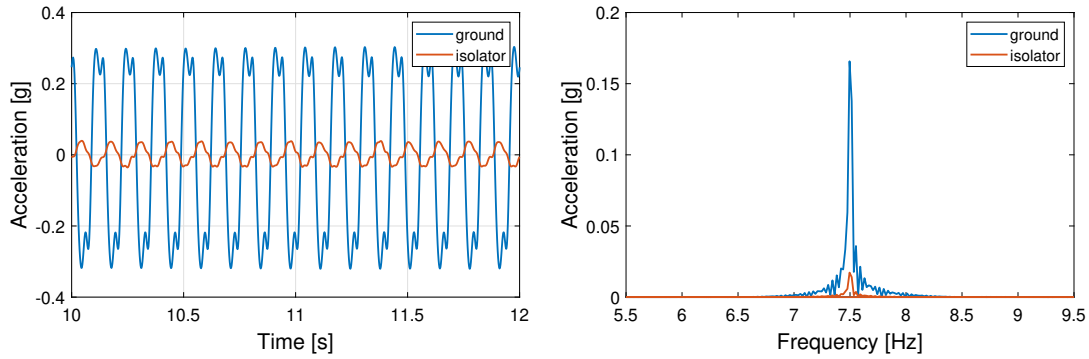

Figure E.8: Acceleration time-history for two-second interval of harmonic test (left) and FFT ±2 Hz of the forcing frequency (right). Test 8 at a frequency of 7.5 Hz and amplitude of 0.30g.

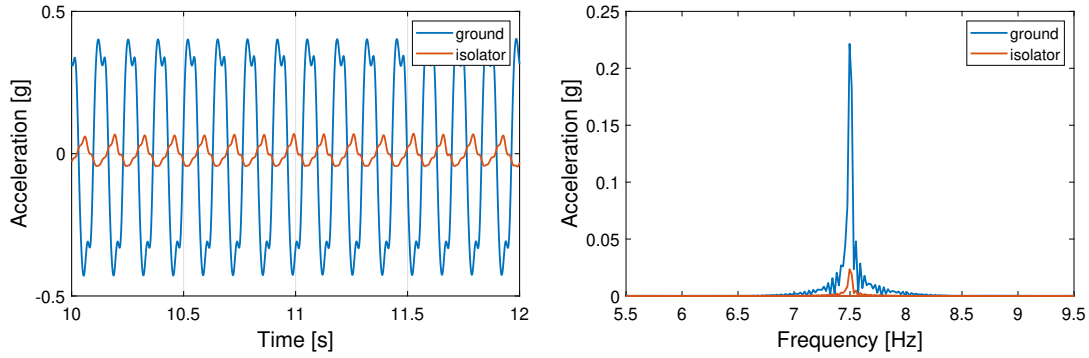

Figure E.9: Acceleration time-history for two-second interval of harmonic test (left) and FFT ±2 Hz of the forcing frequency (right). Test 9 at a frequency of 7.5 Hz and amplitude of 0.40g.

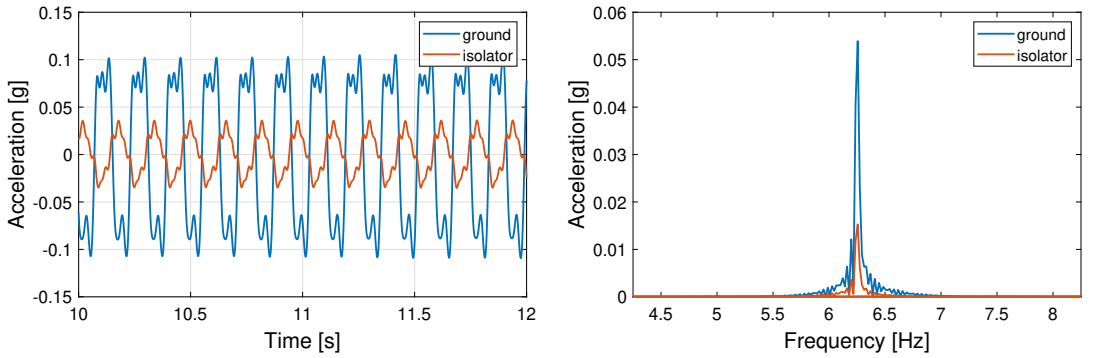

Figure E.10: Acceleration time-history for two-second interval of harmonic test (left) and FFT ±2 Hz of the forcing frequency (right). Test 10 at a frequency of 6.25 Hz and amplitude of 0.10g.

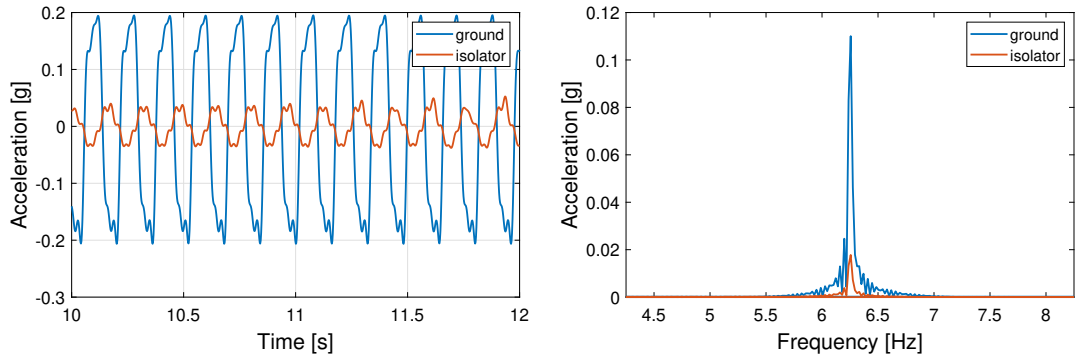

Figure E.11: Acceleration time-history for two-second interval of harmonic test (left) and FFT ±2 Hz of the forcing frequency (right). Test 11 at a frequency of 6.25 Hz and amplitude of 0.20g.

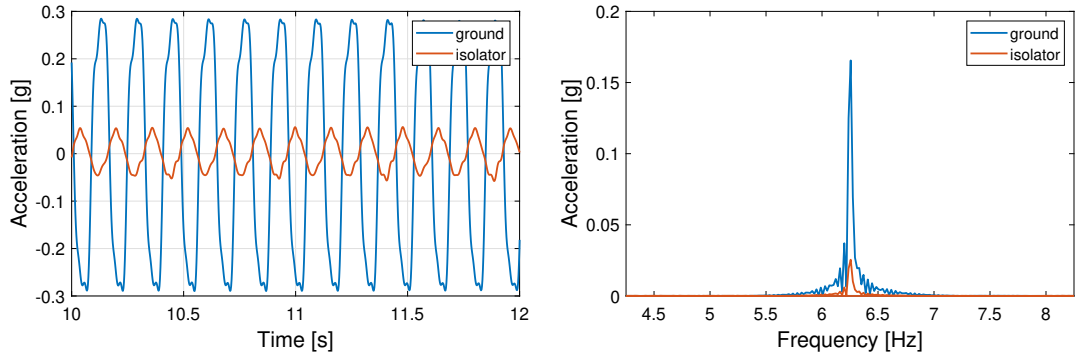

Figure E.12: Acceleration time-history for two-second interval of harmonic test (left) and FFT ±2 Hz of the forcing frequency (right). Test 12 at a frequency of 6.25 Hz and amplitude of 0.30g.

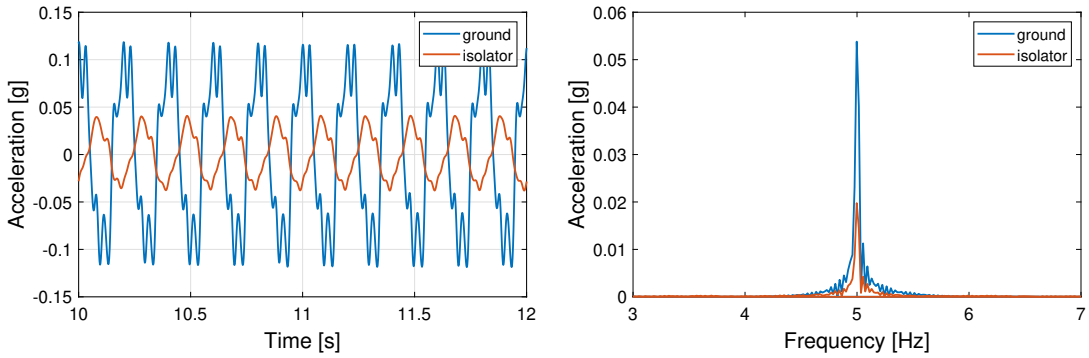

Figure E.13: Acceleration time-history for two-second interval of harmonic test (left) and FFT ±2 Hz of the forcing frequency (right). Test 13 at a frequency of 5 Hz and amplitude of 0.10g.

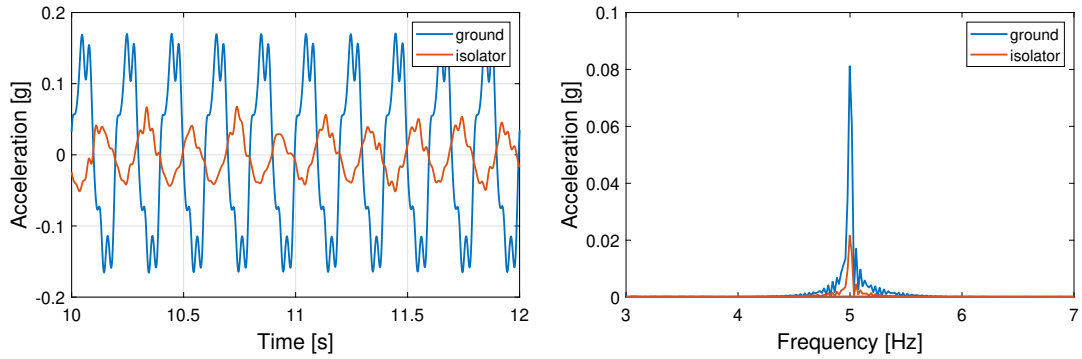

Figure E.14: Acceleration time-history for two-second interval of harmonic test (left) and FFT ±2 Hz of the forcing frequency (right). Test 14 at a frequency of 5 Hz and amplitude of 0.15g.

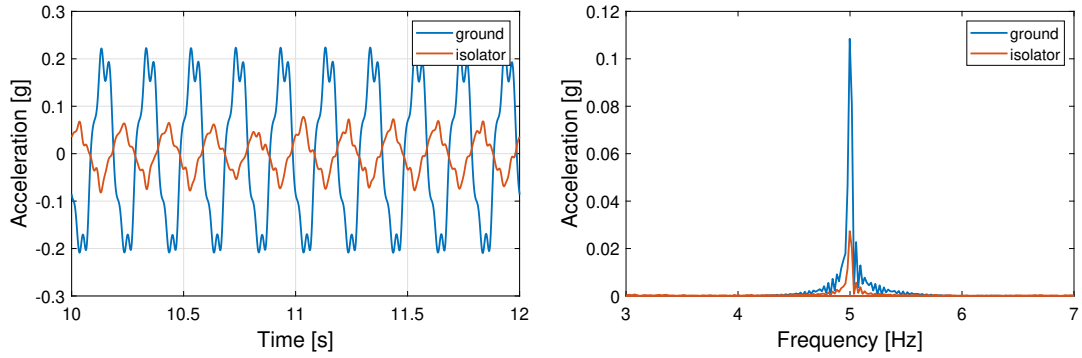

Figure E.15: Acceleration time-history for two-second interval of harmonic test (left) and FFT ±2 Hz of the forcing frequency (right). Test 15 at a frequency of 5 Hz and amplitude of 0.20g.

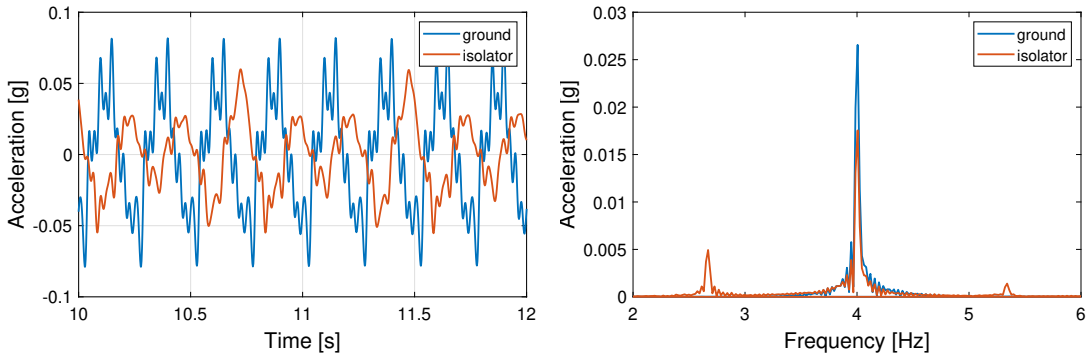

Figure E.16: Acceleration time-history for two-second interval of harmonic test (left) and FFT ±2 Hz of the forcing frequency (right). Test 16 at a frequency of 4 Hz and amplitude of 0.05g.

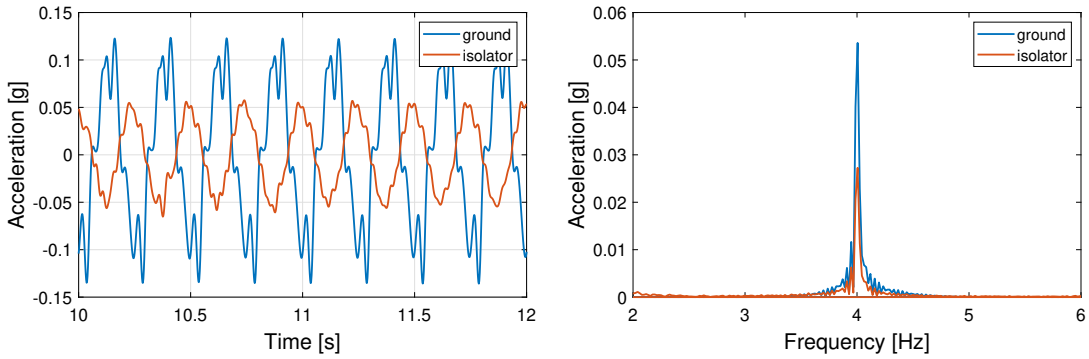

Figure E.17: Acceleration time-history for two-second interval of harmonic test (left) and FFT ± 2 Hz of the forcing frequency (right). Test 17 at a frequency of 4 Hz and amplitude of $0.10g$.

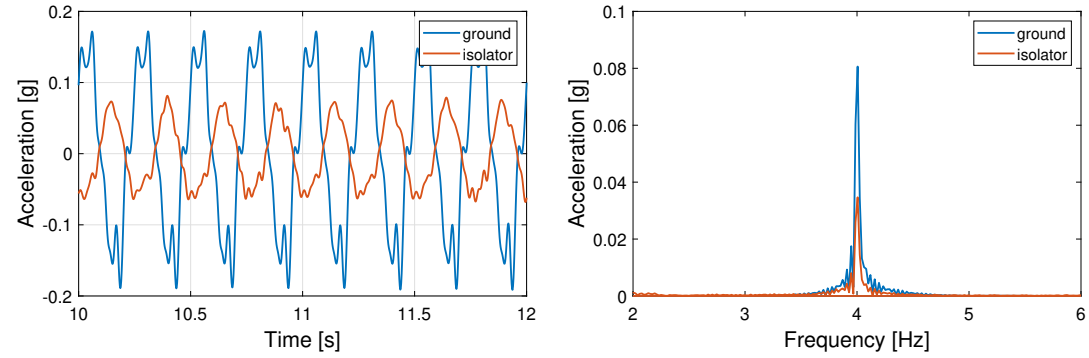

Figure E.18: Acceleration time-history for two-second interval of harmonic test (left) and FFT ± 2 Hz of the forcing frequency (right). Test 18 at a frequency of 4 Hz and amplitude of $0.15g$.

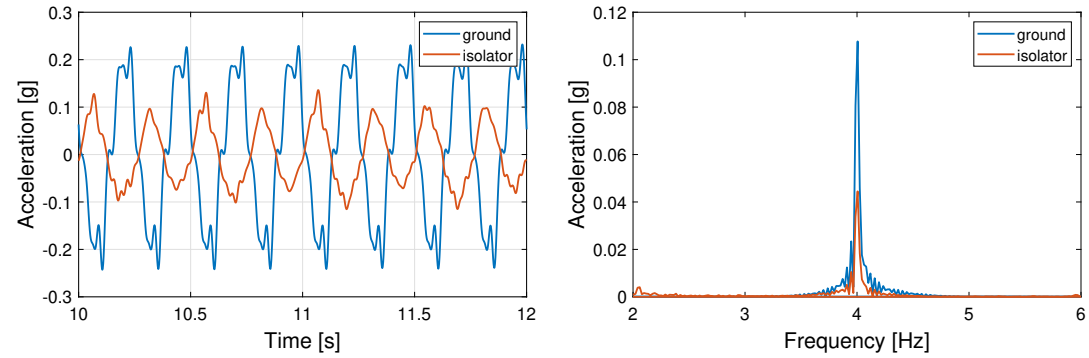

Figure E.19: Acceleration time-history for two-second interval of harmonic test (left) and FFT ± 2 Hz of the forcing frequency (right). Test 19 at a frequency of 4 Hz and amplitude of $0.20g$.

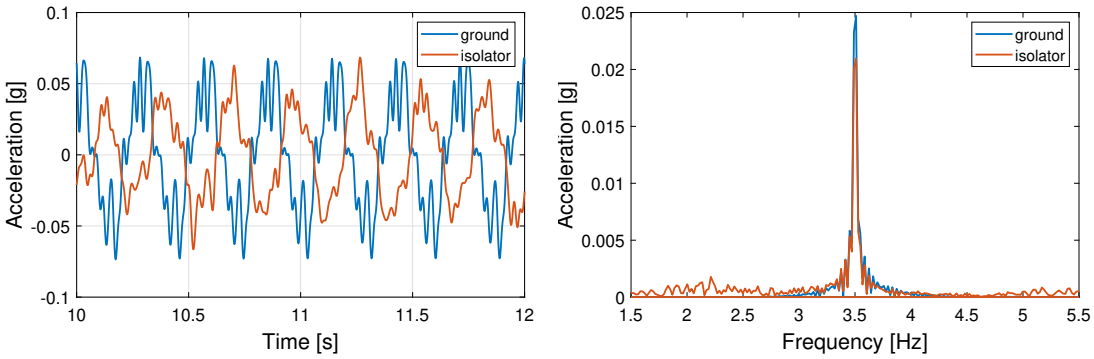

Figure E.20: Acceleration time-history for two-second interval of harmonic test (left) and FFT ±2 Hz of the forcing frequency (right). Test 20 at a frequency of 3.5 Hz and amplitude of 0.05g.

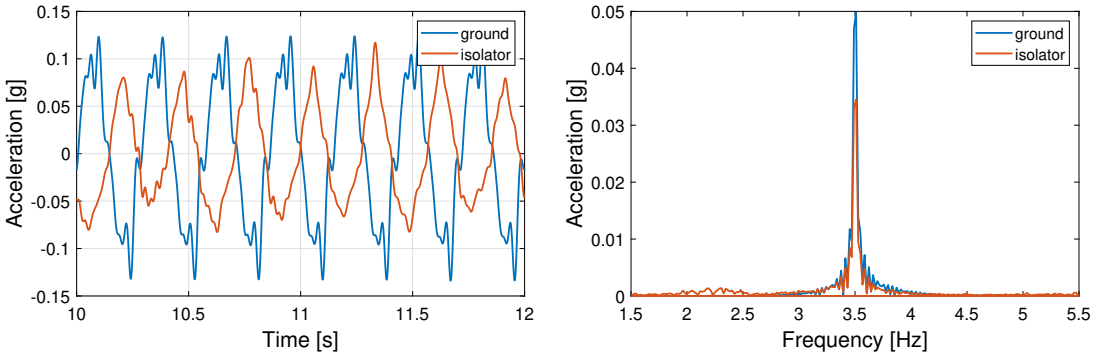

Figure E.21: Acceleration time-history for two-second interval of harmonic test (left) and FFT ±2 Hz of the forcing frequency (right). Test 21 at a frequency of 3.5 Hz and amplitude of 0.10g.

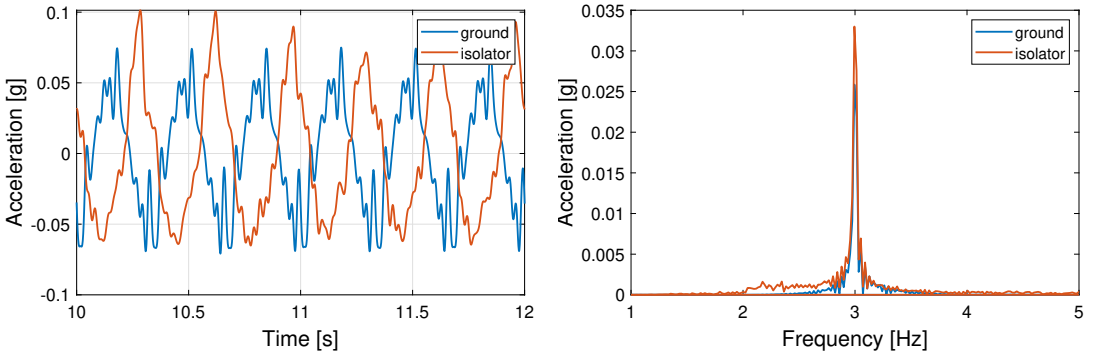

Figure E.22: Acceleration time-history for two-second interval of harmonic test (left) and FFT ±2 Hz of the forcing frequency (right). Test 22 at a frequency of 3 Hz and amplitude of 0.05g.

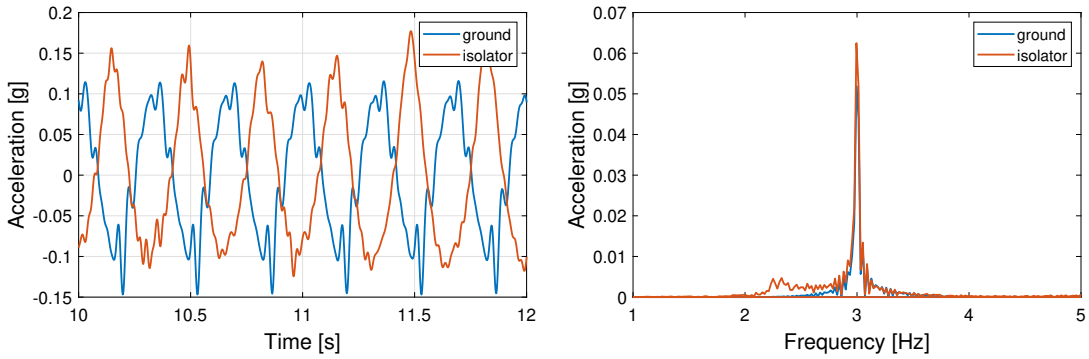

Figure E.23: Acceleration time-history for two-second interval of harmonic test (left) and FFT ±2 Hz of the forcing frequency (right). Test 23 at a frequency of 3 Hz and amplitude of 0.10g.

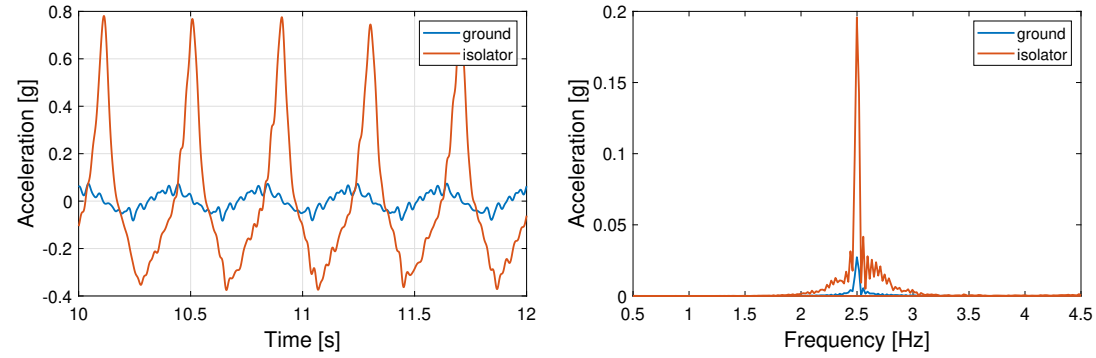

Figure E.24: Acceleration time-history for two-second interval of harmonic test (left) and FFT ±2 Hz of the forcing frequency (right). Test 24 at a frequency of 2.5 Hz and amplitude of 0.05g.

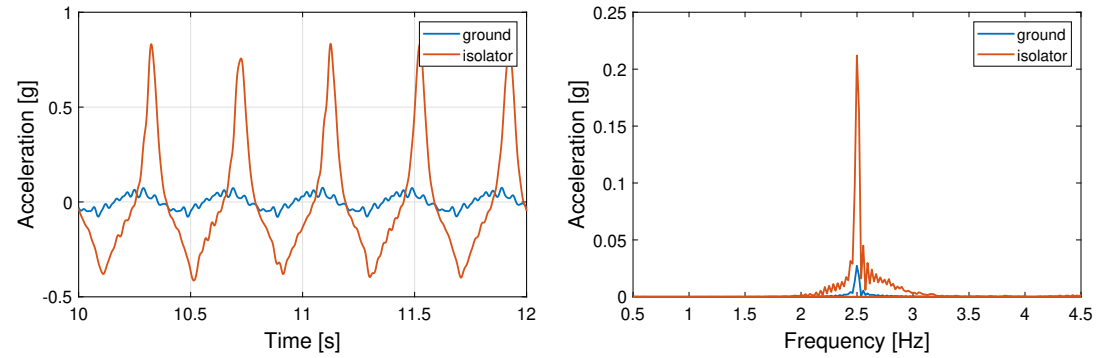

Figure E.25: Acceleration time-history for two-second interval of harmonic test (left) and FFT ±2 Hz of the forcing frequency (right). Test 25 at a frequency of 2.5 Hz and amplitude of 0.05g.

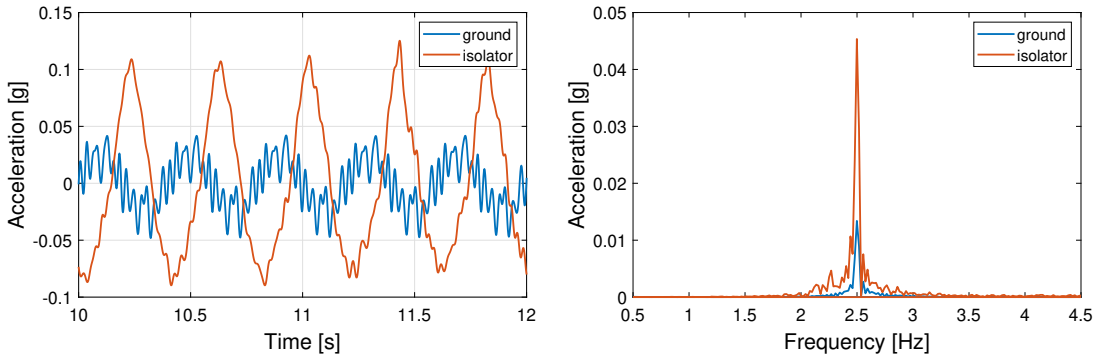

Figure E.26: Acceleration time-history for two-second interval of harmonic test (left) and FFT ±2 Hz of the forcing frequency (right). Test 26 at a frequency of 2.5 Hz and amplitude of 0.025g.

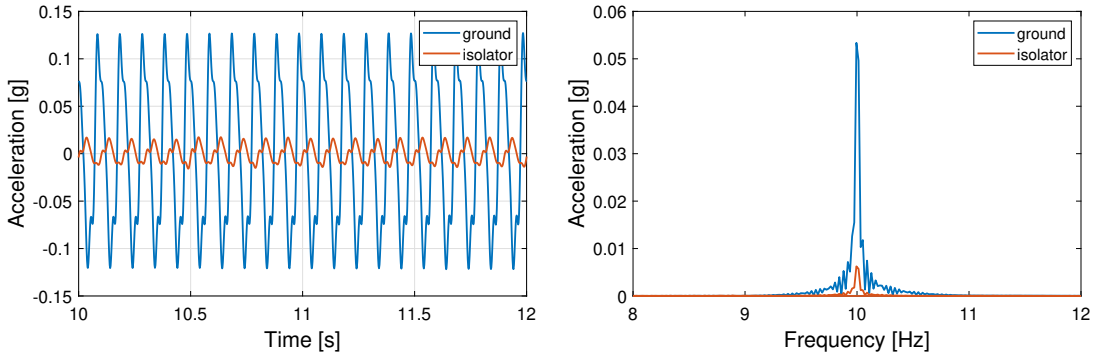

Figure E.27: Acceleration time-history for two-second interval of harmonic test (left) and FFT ±2 Hz of the forcing frequency (right). Test 27 at a frequency of 10 Hz and amplitude of 0.1g.

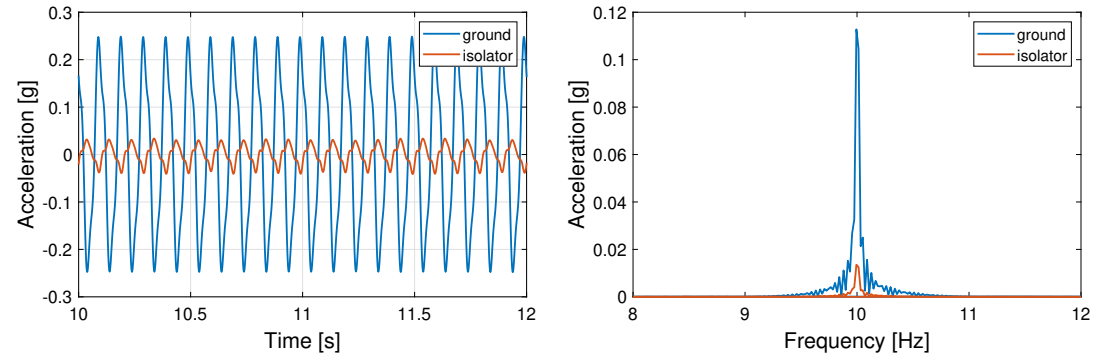

Figure E.28: Acceleration time-history for two-second interval of harmonic test (left) and FFT ±2 Hz of the forcing frequency (right). Test 28 at a frequency of 10 Hz and amplitude of 0.2g.

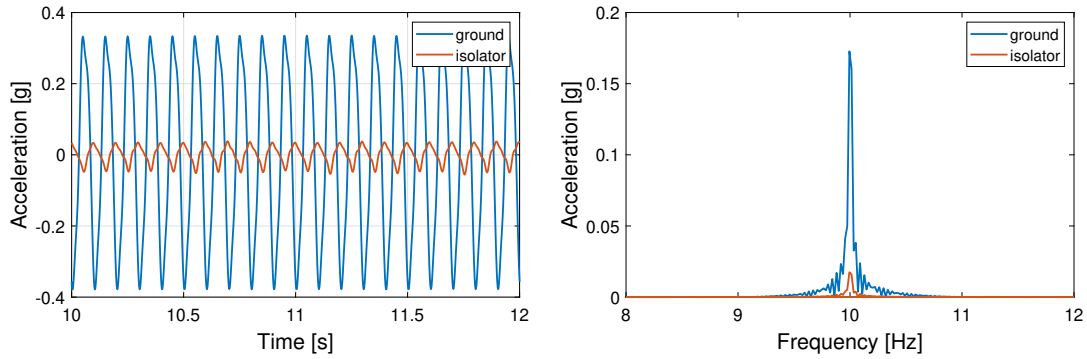

Figure E.29: Acceleration time-history for two-second interval of harmonic test (left) and FFT ±2 Hz of the forcing frequency (right). Test 29 at a frequency of 10 Hz and amplitude of 0.3g.

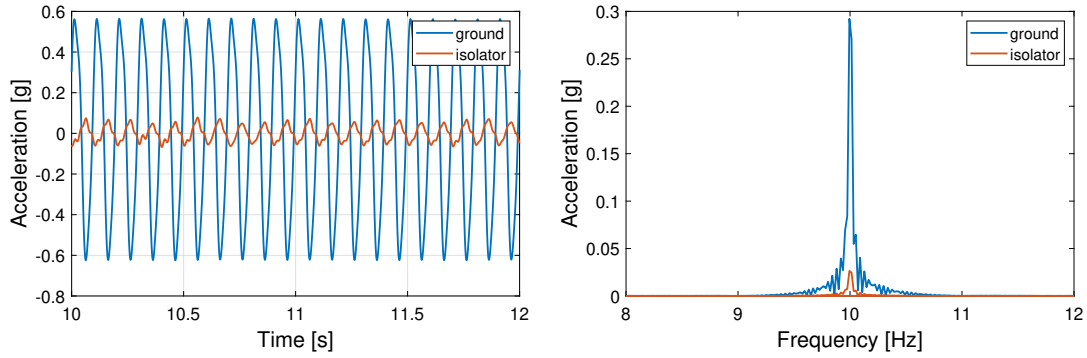

Figure E.30: Acceleration time-history for two-second interval of harmonic test (left) and FFT ±2 Hz of the forcing frequency (right). Test 30 at a frequency of 10 Hz and amplitude of 0.5g.

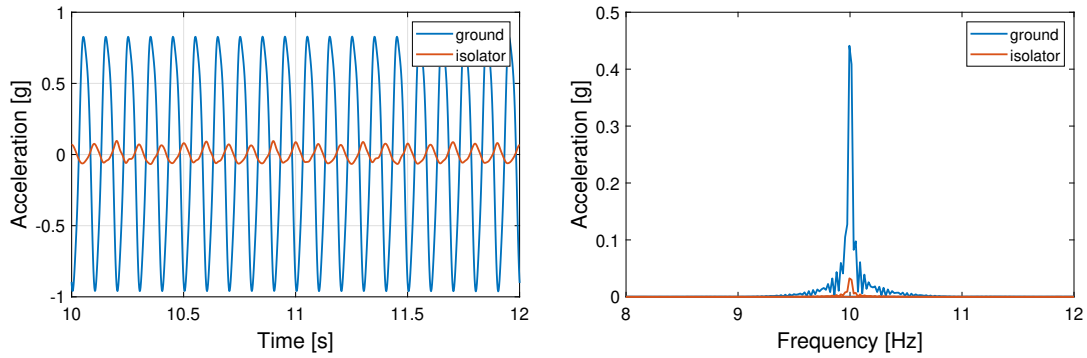

Figure E.31: Acceleration time-history for two-second interval of harmonic test (left) and FFT ±2 Hz of the forcing frequency (right). Test 31 at a frequency of 10 Hz and amplitude of 0.75g.